

Fermion-fermion interaction driven instability and criticality of quadratic band crossing systems with the breaking of time-reversal symmetry

Ya-Hui Zhai and Jing Wang*

Department of Physics, Tianjin University, Tianjin 300072, People's Republic of China

(Dated: December 13, 2021)

We carefully study how the fermion-fermion interactions affect the low-energy states of a two-dimensional spin-1/2 fermionic system on the kagomé lattice with a quadratic band crossing point. With the help of the renormalization group approach, we can treat all kinds of fermionic interactions on the same footing and then establish the coupled energy-dependent flows of fermionic interaction parameters via collecting one-loop corrections, from which a number of interesting results are extracted in the low-energy regime. At first, various sorts of fermion-fermion interactions furiously compete with each other and are inevitably attracted by certain fixed point in the parameter space, which clusters into three qualitatively distinct regions relying heavily upon the structure parameters of materials. In addition, we notice that an instability accompanied by some symmetry breaking is triggered around different sorts of fixed points. Computing and comparing susceptibilities of twelve potential candidates indicates that charge density wave always dominates over all other instabilities. Incidentally, there exist several subleading ones including the x -current, bond density, and chiral plus s -wave superconductors. Finally, we realize that strong fluctuations nearby the leading instability prefer to suppress density of states and specific heat as well compressibility of quasiparticles in the lowest-energy limit.

PACS numbers: 71.10.-w, 71.70.Gm, 71.55.Ak, 64.60.ae

I. INTRODUCTION

Past two decades have witnessed a phenomenally rapid development of semimetal materials [1–12] that feature well-known discrete Dirac points accompanied by gapless quasi-particle excitations and linear energy dispersions along two or three directions [1–9, 12–21]. The list consists of Dirac semimetals [22–27] and Weyl semimetals [2, 28–35] as well as their semi-Dirac cousins [36–41]. In recent years, interest has gradually shifted from linear-dispersion toward quadratic-dispersion fermi materials with up and down bands parabolically touching at certain quadratic band crossing point (QBCP) for both two [42–56] and three dimensions [18, 57–72]. Compared to their Dirac/Weyl counterparts with the vanishment of density of state (DOS) at Dirac points, two-dimensional (2D) QBCP materials attract more attention and become one of the most active subjects [42–44, 47–49, 54, 55]. The main reasons are ascribed to the finite density of states at the Fermi surface together with its unique gapless quasiparticles (QPs) from discrete QBCPs developed by the crossings of up and down parabolical bands, leading to the possibility of weak coupling interaction-driven instability [44, 48, 51, 52]. These 2D QBCP materials are suggested to be realized on some collinear spin density wave state [73], Lieb lattice [74], checkerboard [43, 48] and kagomé lattices [44, 55, 75] with distinct kinds of symmetries under point group consideration [44, 47, 48].

What is more, 2D QBCP systems are allowed to either host the time-reversal symmetry (TRS) or present

the TRS breaking depending upon concrete lattices. On one side, the free Hamiltonian of 2D QBCP semimetals rooted in the checkerboard lattice is protected by TRS [44, 47, 48]. With respect to these materials, unconventional band structures and gapless QPs in tandem with weak couplings yield to many interesting behaviors in the low-energy regime [44–46, 48, 50, 51, 76, 77]. In particular, quantum anomalous Hall (QAH) and quantum spin Hall (QSH) can be generated by fermion-fermion repulsive interactions on the checkerboard lattice [44, 48] or two-valley bilayer graphene with QBCPs [45, 46], as well as their low-energy stabilities under the impacts of impurity scatterings are also examined [51, 52]. On the other side, the 2D noninteracting QBCP model that originates from the kagomé lattice might be TRS breaking [75]. Although this case is equipped with the similar QBCP and quadratic dispersion, its low-energy physics has hitherto been insufficiently explored. Given the basic structure of free Hamiltonian is quite far away from its checkerboard counterpart, a number of tempting questions concerning the kagomé-lattice version naturally arise: whether and how the low-energy physical properties are influenced by fermion-fermion interaction? Whether they can activate the instabilities? Which states are the suitable candidates and what are the critical behaviors in the vicinity of potential instabilities? It would be instructive to deepen our understanding of the 2D QBCP materials once these inquiries are properly answered.

Inspired by these, we within this work put our focus on a 2D QBCP spin-1/2 fermionic system on the kagomé lattice and investigate its low-energy fate in the presence of 16 types of marginal fermion-fermion interactions. In order to treat all these physical ingredients on an equal

*Corresponding author: jing_wang@tju.edu.cn

footing, we employ the momentum-shell renormalization-group (RG) approach [78–80], which is a powerful tool to refine and characterize the hierarchical physics in the simultaneous presence of various types of interactions. Practicing the standard procedures of RG framework gives rise to the one-loop energy-dependent evolutions of all fermion-fermion interaction parameters. With the help of these RG flows that encode the energy-dependent physics, several intriguing critical behaviors are extracted in the low-energy regime.

At first, we, with the help of the numerical analysis of RG equations, are aware that the fermion-fermion interactions are of close relevance to each other and evolve towards strong couplings due to their intimate interplay at certain energy scale. Considering the degenerate trajectories of several kinds of interactions, we only need to put our focus on six nontrivial fermionic couplings that flow independently. To overcome the strong couplings and make our study perturbative, we follow the strategy put forward in Refs. [45, 48] and then rescale these six nontrivial parameters by a non-sign changed coupling to obtain their relative evolutions together with relatively fixed points which are conventionally in charge of low-energy properties.

Next, we figure out that the concrete values of relatively fixed points are insusceptible to initial conditions of fermion-fermion interactions but instead primarily determined by two structure parameters d_1 and d_3 in the Hamiltonian. Adjusting the ratio between these two quantities yields to three qualitative different regions at which the relatively fixed points exhibit diverse traits. Since the relatively fixed point is related to some instability that is always accompanied by certain symmetry breaking and thus some phase transition [47, 48, 51, 81–88], it is therefore of intense interest to identify which is the leading instability for the relatively fixed point residing in different regions. To this end, we introduce the source terms of twelve kinds of potential candidates and evaluate their related susceptibilities approaching a relatively fixed point [47, 48, 51]. Carrying out both the theoretical and numerical analysis indicates that the charge density wave always takes a leading role in the whole region. In addition, four subleading ones involving the x -current, bond density, and chiral or s -wave superconductors largely hinge upon the relatively fixed points.

Moreover, the critical properties of physical implications are briefly studied around the leading instability. It is worth pointing out that these quantities are sensitive to the fluctuation of order parameter triggered by the dominant instability. We notice that ferocious fluctuations induced by the development of charge density wave are generally detrimental to the density of states and specific heat as well compressibility of quasiparticles. Especially, they are all substantially reduced and even drive to zero as the leading instability is accessed [82, 89–94].

The rest of paper is organized as follows. In Sec II A, we present the microscopic model for a 2D QBCP spin-1/2 electronic system on the kagomé lattice and construct

our effective action consisting of both free terms and all marginal fermion-fermion interactions. Starting from this effective theory, we within Sec. II B carry out one-loop momentum-shell RG analysis and derive the coupled RG equations of all fermionic interaction parameters. By virtue of numerical analysis of RG evolutions, Sec. III is followed to seek and classify the underlying fixed points in the low-energy regime. In addition, we bring out the source terms in Sec. IV and pinpoint the dominant and subleading instabilities nearby distinct types of relatively fixed points. Furthermore, several critical behaviors of physical quantities activated by ferocious fluctuations are concisely investigated in Sec. V. Finally, Sec. VI briefly summarizes our central points.

II. EFFECTIVE THEORY AND RG ANALYSIS

At the outset, we are going to present the microscopic model and build the effective theory in the low-energy regime as well as establish the coupled energy-dependent flow equations of all marginal fermion-fermion couplings by carrying out the standard momentum-shell RG framework [78–80].

A. Effective theory

We hereafter concentrate on the 2D spin-1/2 electronic system stemming from the kagomé lattice that is characterized by a QBCP at which up and down energy bands parabolically meet [44, 75]. Accordingly, its non-interacting Hamiltonian that captures the low-energy fermionic excitations nearby the QBCP can be written as [44, 75],

$$H_0 = \sum_{|\mathbf{k}| < \Lambda} \Psi_{\mathbf{k}}^{\dagger} \mathcal{H}_0(\mathbf{k}) \Psi_{\mathbf{k}}, \quad (1)$$

where Λ serves as the momentum cutoff and the Hamiltonian density is cast as [75]

$$\mathcal{H}_0(\mathbf{k}) = d_3 \mathbf{k}^2 \Sigma_{03} + d_1 (k_x^2 - k_y^2) \Sigma_{01} + d_2 k_x k_y \Sigma_{02}, \quad (2)$$

with d_1 , d_2 , and d_3 being microscopic structure parameters of continuum Hamiltonian. Hereby, $\Psi_{\mathbf{k}}^{\dagger} = (c_{1\uparrow}^{\dagger}, c_{1\downarrow}^{\dagger}, c_{2\uparrow}^{\dagger}, c_{2\downarrow}^{\dagger})$ is designated as a four-component spinor to specify the low-energy quasiparticles coming from two energy bands and unequal spins [44, 75]. In addition, the 4×4 matrix $\Sigma_{\mu\nu} \equiv \tau_{\mu} \otimes \sigma_{\nu}$, where τ_{μ} and σ_{ν} with $\mu, \nu = 0, 1, 2, 3$ represent Pauli matrices $\tau_{1,2,3}$, $\sigma_{1,2,3}$ and identity matrix τ_0 , σ_0 , is employed to act on both the spin space and lattice space. Diagonalizing the free Hamiltonian (2) straightforwardly gives rise to the parabolical energy eigenvalues,

$$E = \left\{ \pm d_3 \mathbf{k}^2, \pm \mathbf{k}^2 \sqrt{d_3^2 + d_1^2 \cos^2 2\theta_{\mathbf{k}} + \frac{1}{4} d_2^2 \sin^2 2\theta_{\mathbf{k}}} \right\}, \quad (3)$$

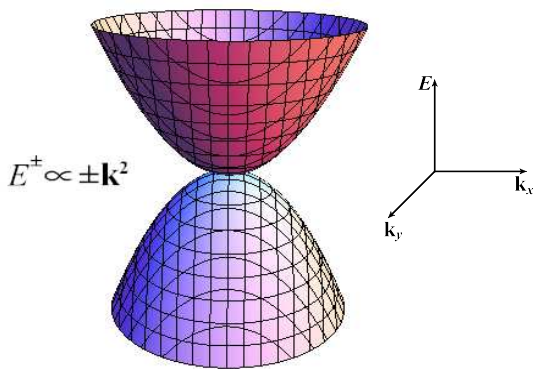


FIG. 1: (Color online) Schematic illustration of the 2D QBCP band structure with a quadratic band crossing point parabolically touched by the up and down energy bands.

where \pm specify the upward and downward energy bands that quadratically touch at $\mathbf{k} = 0$ as schematically shown in Fig. 1 and $\theta_{\mathbf{k}} \equiv \arctan(k_y/k_x)$ measures the direction of momentum \mathbf{k} . It is of particular interest to point out that the presence of $\theta_{\mathbf{k}}$ points to rotational asymmetry of the QBCP system, and its counteraction with the restriction of $d_2 = 2d_1$ signals an indication of rotational invariance. Within this work, we put our focus on the 2D QBCP semimetal owning the rotational symmetry. To this end, taking $d_2 = 2d_1$ yields the reduced energy eigenvalues as

$$E^\pm(\mathbf{k}) = \pm \mathbf{k}^2 \sqrt{d_1^2 + d_3^2}. \quad (4)$$

$$S_{\text{eff}} = \int_{-\infty}^{\infty} \frac{d\omega}{2\pi} \int \frac{d^2\mathbf{k}}{(2\pi)^2} \Psi^\dagger(\omega, \mathbf{k}) [-i\omega \Sigma_{00} + d_3 \mathbf{k}^2 \Sigma_{03} + d_1(k_x^2 - k_y^2) \Sigma_{01} + d_2 k_x k_y \Sigma_{02}] \Psi(\omega, \mathbf{k}) + \sum_{\mu, \nu=0}^3 \lambda_{\mu\nu} \int_{-\infty}^{\infty} \frac{d\omega_1 d\omega_2 d\omega_3}{(2\pi)^3} \\ \times \int \frac{d^2\mathbf{k}_1 d^2\mathbf{k}_2 d^2\mathbf{k}_3}{(2\pi)^6} \Psi^\dagger(\omega_1, \mathbf{k}_1) \Sigma_{\mu\nu} \Psi(\omega_2, \mathbf{k}_2) \Psi^\dagger(\omega_3, \mathbf{k}_3) \Sigma_{\mu\nu} \Psi(\omega_1 + \omega_2 - \omega_3, \mathbf{k}_1 + \mathbf{k}_2 - \mathbf{k}_3). \quad (6)$$

On the basis of quantum field theory, its noninteracting part directly gives rise to the free fermionic propagator [78]

$$G_0(i\omega, \mathbf{k}) = \frac{1}{-i\omega + d_3 \mathbf{k}^2 \Sigma_{03} + d_1(k_x^2 - k_y^2) \Sigma_{01} + d_2 k_x k_y \Sigma_{02}}, \quad (7)$$

which plays a crucial role in constructing the RG equations.

We hereafter adopt the S_{eff} as our starting point and utilize the RG approach to inspect the low-energy behaviors of 2D spin-1/2 QBCP electric systems sitting on the kagomé lattice in the presence of these marginal fermion-fermion interactions.

As aforementioned, it has attracted much interest to investigate the impacts of fermion-fermion interactions on the low-energy fates of 2D QBCP systems locating at checkerboard lattices [44, 45, 48, 51, 52, 95, 96]. However, compared to its checkerboard counterpart [43, 48], we need to bear in mind that the 2D QBCP model (2) with the TRS breaking is still inadequately explored despite of holding the particle-hole symmetry and sixfold rotational symmetry [44, 75]. Due to the qualitative difference of microscopic structures between kagomé and checkerboard lattices, we therefore within this work endeavor to verify how the fermion-fermion interactions impact the low-energy properties of 2D kagomé-version QBCP systems.

To be concrete, we herein take into account all potential marginal short-range four-fermion interactions on an equal footing [44, 48, 51, 75]

$$S_{\text{int}} = \sum_{\mu, \nu=0}^3 \lambda_{\mu\nu} \prod_{i=1}^3 \int \frac{d\omega_i d^2\mathbf{k}_i}{(2\pi)^3} \Psi^\dagger(\omega_1, \mathbf{k}_1) \Sigma_{\mu\nu} \Psi(\omega_2, \mathbf{k}_2) \\ \times \Psi^\dagger(\omega_3, \mathbf{k}_3) \Sigma_{\mu\nu} \Psi(\omega_1 + \omega_2 - \omega_3, \mathbf{k}_1 + \mathbf{k}_2 - \mathbf{k}_3), \quad (5)$$

where $\lambda_{\mu\nu}$ with $\mu, \nu = 0, 1, 2, 3$ are utilized to measure the coupling strengths of different types of fermion-fermion interactions that are distinguished by vertex matrixes $\Sigma_{\mu\nu}$ acting on both lattice and spin spaces.

Consequently, we are left with the effective action in the momentum space after combining the free Hamiltonian (1) and fermion-fermion interactions (5) as follows [44, 48, 51]

B. RG analysis

We within this subsection implement the one-loop momentum-shell RG analysis [78–80] to construct the entangled energy-dependent evolutions of all interaction parameters appearing in Eq. (6) that are of close relevance to the low-energy properties.

Prior to deriving the one-loop RG equations, we are forced to determine the rescaling transformations of momentum, energy, and fields [78]. To this end, we can select the non-interacting parts of effective action (6) as an original fixed point at which they are invariant during RG processes. As a result, we obtain the following RG

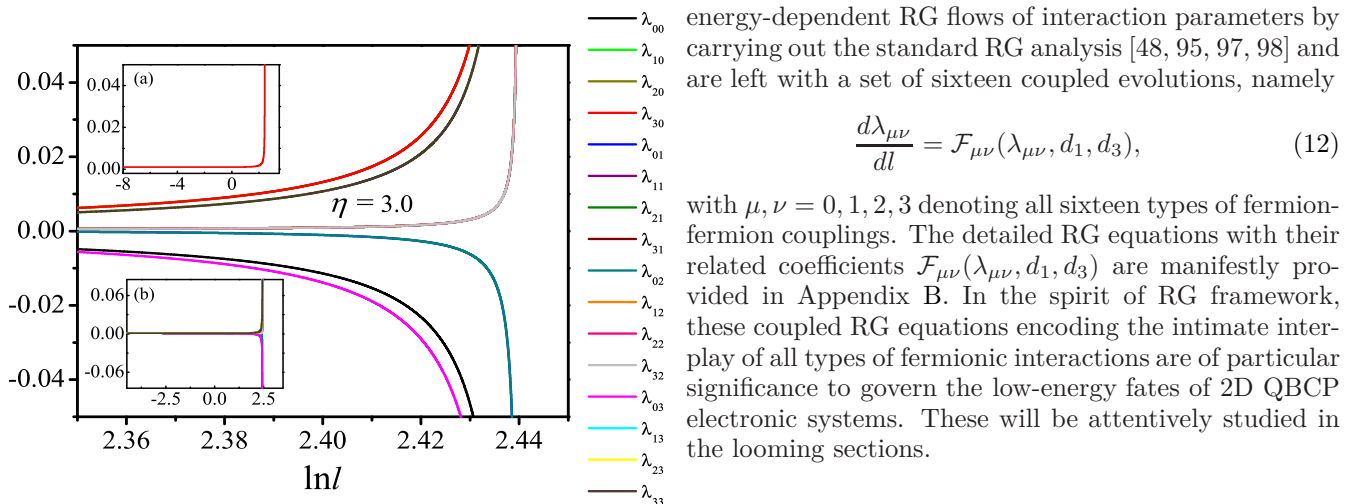


FIG. 2: (Color online) Evolutions of fermion-fermion couplings $\lambda_{\mu\nu}$ at the ratio of structure parameters $\eta = 3.0$ (the basic results are insensitive to concrete value of η). Insets: (a) the flows of $\lambda_{\mu\nu}$ in the whole energy region, and (b) the flow of λ_{30} without sign change under the influence of fermion-fermion interactions.

rescaling transformations [48, 95, 97, 98]

$$k_x \longrightarrow k'_x e^{-l}, \quad (8)$$

$$k_y \longrightarrow k'_y e^{-l}, \quad (9)$$

$$\omega \longrightarrow \omega' e^{-2l}, \quad (10)$$

$$\Psi(i\omega, \mathbf{k}) \longrightarrow \Psi'(i\omega', \mathbf{k}') e^{3l}. \quad (11)$$

In order to grasp the contributions from fermion-fermion interactions, we have to go beyond this original fixed point and take into account all one-loop corrections. In the spirit of momentum-shell RG theory [78], the “fast modes” of fermionic fields within the momentum shell $b\Lambda < k < \Lambda$ are integrated out at first, where Λ characterizes the energy scale and variable b is designated as $b = e^{-l} < 1$. It is worth highlighting that l serves as a running length scale and thus its increase is equivalent to the decrease of energy scale. Next, we insert the corrections within the momentum shell into the “slow modes” to yield the new “slow modes” and then rescale these “slow modes” to new “fast modes” [47, 48, 51, 81, 95, 97–103]. In principle, it is convenient to measure the momenta and energy with cutoff Λ_0 which is related to the lattice constant (i.e., $k \rightarrow k/\Lambda_0$ and $\omega \rightarrow \omega/\Lambda_0$) to simplify our calculations and write the results more compactly [48, 95, 97, 98, 100, 104]. To be specific, we unbiasedly take into account all one-loop Feynman diagrams depicted in Fig. 12 to capture the one-loop information of “fast modes”. After paralleling the well-trodden procedures and performing long but straightforward algebra [48, 51, 95, 95, 96], all one-loop corrections are obtained and presented detailedly in Appendix A.

Combining RG rescalings (8)-(11) and one-loop corrections (A1)-(A16), we are capable of deriving the coupled

energy-dependent RG flows of interaction parameters by carrying out the standard RG analysis [48, 95, 97, 98] and are left with a set of sixteen coupled evolutions, namely

$$\frac{d\lambda_{\mu\nu}}{dl} = \mathcal{F}_{\mu\nu}(\lambda_{\mu\nu}, d_1, d_3), \quad (12)$$

with $\mu, \nu = 0, 1, 2, 3$ denoting all sixteen types of fermion-fermion couplings. The detailed RG equations with their related coefficients $\mathcal{F}_{\mu\nu}(\lambda_{\mu\nu}, d_1, d_3)$ are manifestly provided in Appendix B. In the spirit of RG framework, these coupled RG equations encoding the intimate interplay of all types of fermionic interactions are of particular significance to govern the low-energy fates of 2D QBCP electronic systems. These will be attentively studied in the looming sections.

III. RELATIVE FIXED POINTS

With the coupled RG flow equations in hand, we are able to seek the underlying fixed points with lowering the energy scales, which are always assumed to dictate the critical behaviors.

A. Evolutions of interaction parameters

We start out by investigating the energy-dependent flows of four-fermion couplings, which are determined by RG equations and assumed to overarch the low-energy properties [47, 48, 51, 81, 95, 97–103]. Before proceeding, it is necessary to present several comments on the initial condition. On one hand, we, without loss of generality, treat all sixteen types of marginal fermion-fermion interactions unbiasedly and assign them an equal beginning value. On the other hand, the RG coupled equations also rely upon two structural parameters d_1 and d_3 . It is of particular importance to highlight that the flows of interaction parameters are insensitive to their concrete values but instead the ratio between d_1 and d_3 . To facilitate our analysis, we hereafter designate $\eta \equiv d_3/d_1$ to capture the basic influence of these two parameters.

To proceed, taking a concrete value $\eta = 3.0$ plus a representative starting value for $\lambda_{\mu\nu}$ and performing numerical analysis of Eq. (12), we are left with the results shown in Fig. 2. Reading off this figure, we notice that fermion-fermion interactions are strongly energy-dependent and driven to be divergent at some critical energy scale denoted by l_c in the low-energy regime, which always is an unambiguous signature for the emergence of phase transitions [47, 48, 51, 81–88]. In addition, after completing numerical calculations of coupled RG evolutions of interactions parameters (B1)-(B16), we figure out that six groups of interaction parameters are not coincident and their trajectories do not overlap with decreasing the energy scale as depicted in Fig. 2. To be concrete, λ_{01} is

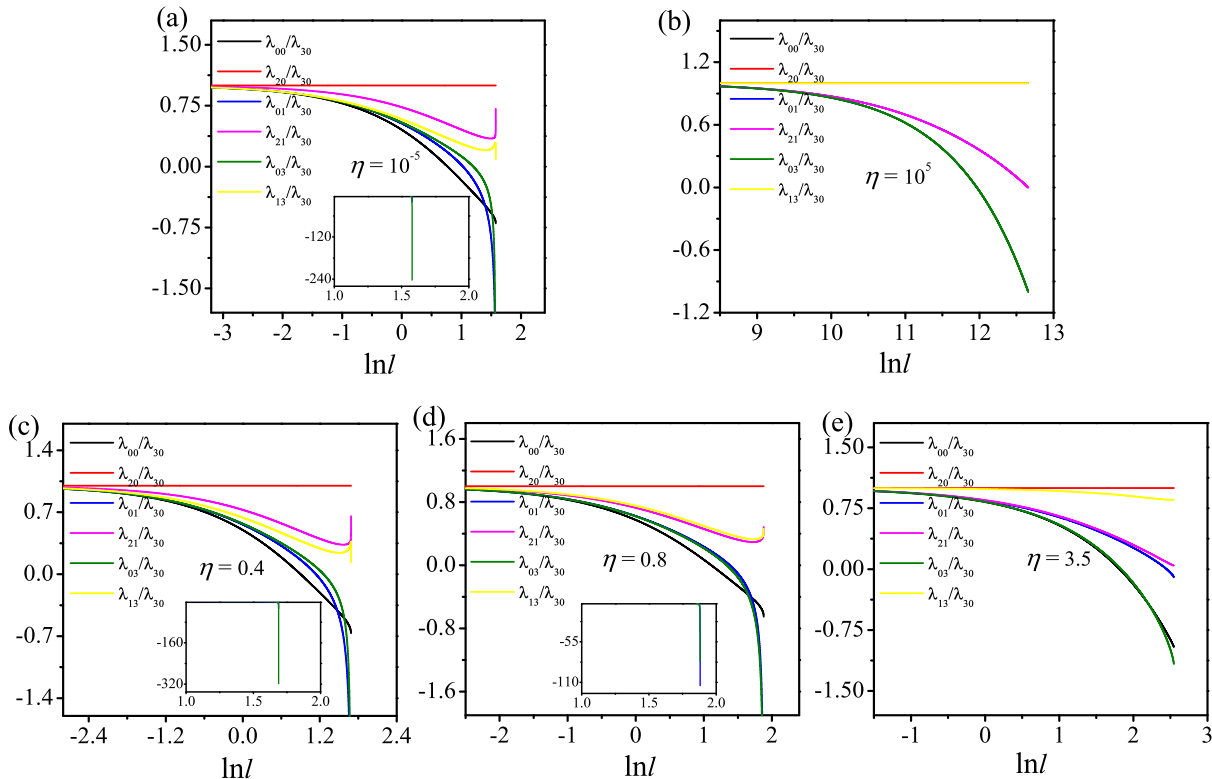


FIG. 3: (Color online) Evolutions for six representative sorts of fermion-fermion interaction parameters $\lambda_{\mu\nu}/\lambda_{30}$ with approaching: (a) Type-I-RFP at $\eta = 10^{-5}$; (b) Type-III-RFP at $\eta = 10^5$; and (c)-(e) Type-II-RFP at $\eta = 0.4$, $\eta = 0.8$, and $\eta = 3.5$, respectively.

degenerate with λ_{02} and λ_{13} is coincident to λ_{23} plus λ_{33} , respectively. In particular, the tendencies of parameters λ_{10} , λ_{20} , and λ_{30} are exactly overlapped. Analogously, λ_{11} , λ_{21} , λ_{31} , λ_{12} , λ_{22} , and λ_{32} share the same evolution. These imply that some of these 16 kinds of interaction parameters may be not independent. As a result, all of these 16 kinds of interaction parameters can be clustered into six groups. In order to compactly exhibit the flow trajectories of interaction parameters and simplify our discussions, we therefore from now on choose four representative parameters λ_{01} , λ_{20} , λ_{21} , and λ_{13} to denote their degenerate counterparts. In other words, there only exist six independent flows λ_{00} , λ_{20} , λ_{01} , λ_{21} , λ_{03} , and λ_{13} that are employed to characterize all types of fermion-fermion interactions.

B. Three η -dependent distinct regions

In light of the divergence of fermion-fermion couplings in the low-energy regime, we are conventionally suggested to rescale all parameters with a non-sign changed parameter [45, 48, 51]. Based on the relative interaction parameters, one henceforth can safely work within the perturbative RG framework before the divergence [45, 48, 51, 81–88].

As explicitly illustrated by Fig. 2(a), the parameter λ_{30}

flows monotonously and thus does not change sign during the entire RG flow. It is therefore convenient to measure all interaction parameters with λ_{30} . Accordingly, we from now on shift our attention to the low-energy behaviors of these relative parameters, i.e., $\lambda_{00}/\lambda_{30}$, $\lambda_{20}/\lambda_{30}$, $\lambda_{01}/\lambda_{30}$, $\lambda_{21}/\lambda_{30}$, $\lambda_{03}/\lambda_{30}$, and $\lambda_{13}/\lambda_{30}$. Besides their energy-dependent trajectories, we are of particular interest to determine the final fates of these parameters at the low-energy limit, namely, the potential fixed point (FP) which is expected to govern the physical properties and accompanied by critical behaviors. Given these parameters are rescaled by λ_{30} , we hereafter dub them relatively fixed points (RFPs) [45, 48, 51].

Although the basic results are hardly susceptible to starting values of fermion-fermion strengths, the flows of interaction parameters and corresponding RFPs are heavily η -dependent. Fig. 3 manifestly shows the evolving tendencies of fermion-fermion interaction parameters strongly hinge upon the specific values of η . What is more, we learning from Fig. 4 notice that concrete values of RFPs are closely sensitive to η as well. On one side, as long as η is either tuned less than certain small value nominated as C_1 or adjusted to exceed some critical value denoted as C_2 , the final values of parameters $\lambda_{\mu\nu}/\lambda_{30}$ (i.e., RFPs) arrive at some constants and then are considerably robust with lowering or increasing value

TABLE I: Specific values of fermion-fermion interactions with several representative ratios of structure parameters in the vicinity of three different RFPs. The corresponding energy-dependent evolutions of these couplings are manifestly displayed in Fig. 3.

RFPs	$\lambda_{00}/\lambda_{30}$	$\lambda_{20}/\lambda_{30}$	$\lambda_{01}/\lambda_{30}$	$\lambda_{21}/\lambda_{30}$	$\lambda_{03}/\lambda_{30}$	$\lambda_{13}/\lambda_{30}$	η
Type-I-RFP	-0.7	1	-20.3	0.7	-242.8	0.1	10^{-5}
Type-II-RFP	-0.7	1	-28.4	0.7	-318.1	0.1	0.4
	-0.7	1	-114.5	0.5	-81	0.5	0.8
Type-III-RFP	-1	1	-0.1	0.04	-1.2	0.9	3.5
	-1	1	0	0	-1	1	10^5

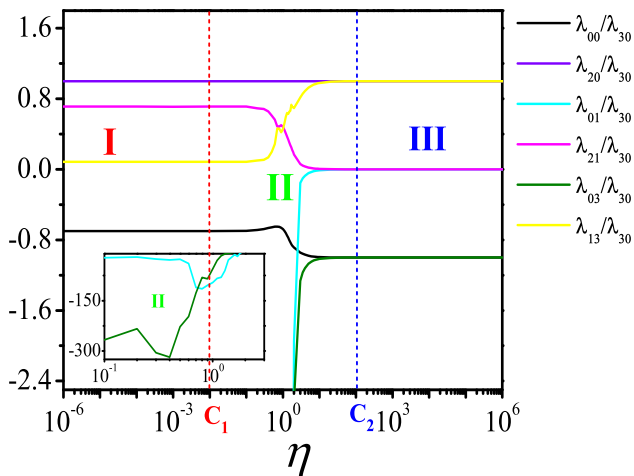


FIG. 4: (Color online) The η -dependent evolutions of fermion-fermion interaction parameters $\lambda_{\mu\nu}/\lambda_{30}$ (i.e., the concrete values of RFPs). Three distinct regions are separated by $\eta = C_1 \approx 10^{-2}$ and $\eta = C_2 \approx 10^2$, which are denominated as Type-I-Region, Type-II-Region, Type-III-Region (namely, I, II, and III), respectively.

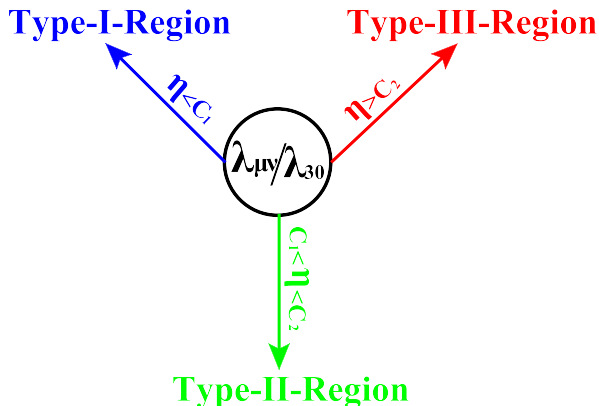


FIG. 5: (Color online) Schematic illustration of three different η -tuned regions shown in Fig. 4 with $C_1 \approx 10^{-2}$ and $C_2 \approx 10^2$. Several representative values of RFPs are presented in Table I for Type-I-Region, Type-II-Region, and Type-III-Region, respectively.

of η . On the other side, the concrete values of RFPs spanning from C_1 to C_2 are no longer invariant but instead fairly rely upon η . For physical consideration, we infer that d_1 is dominant over d_3 at $\eta < C_1$ and thus the contribution from d_3 is negligible resulting in the stable values of RFPs and vice versa for $\eta > C_2$. On the contrary, neither d_1 nor d_3 can completely win its opponent within $C_1 < \eta < C_2$. It is thus the intimate competition between d_1 and d_3 that plays a pivotal role in pinning down RFPs as unambiguously characterized in Fig. 4.

To be specific, we directly notice that the absolute values of negative-divergent parameters $\lambda_{01}/\lambda_{30}$ and $\lambda_{03}/\lambda_{30}$ as well as the positive-divergent parameter $\lambda_{21}/\lambda_{30}$ present a clear downward trend with increasing the values of η . Conversely, the increase of η is favorable to raise the absolute value of negative-divergent parameter $\lambda_{00}/\lambda_{30}$ together with positive-divergent parameters $\lambda_{13}/\lambda_{30}$. In comparison, one can readily figure out $\lambda_{20}/\lambda_{30} = 1$ is hardly susceptible to the modulation of η . In order to facilitate our studies under such circumstances, it is profitable to divide $\eta \in (0, \infty)$ into three distinct regions owing to the robustness of RFPs against the change of η . As manifestly designated in Fig. 4 and schematically illustrated in Fig. 5, they correspond to Type-I-Region ($\eta < C_1$), Type-II-Region ($C_1 < \eta < C_2$), and Type-III-Region ($\eta > C_2$), respectively.

C. Three types of relatively fixed points

Concerning the discrepancies of RFPs in these three regions, we from now on nominate the RFPs locating at Type-I-Region, Type-II-Region, and Type-III-Region as Type-I-RFP, Type-II-RFP, Type-III-RFP, respectively. In order to remedy the insufficiency of qualitative illustrations in Fig. 5, we hereby select some representative values of η with three different types of RFPs and present the specific values of the interaction parameters as collected in Table I apparently indicating their individual features. As aforementioned, the final values of interaction parameters manifested in Fig. 4 are stable in Type-I-Region and Type-III-Region under the variation of η . On the contrary, they are rather sensitive to η in the Type-

TABLE II: Twelve different kinds of potential phases triggered by fermion-fermion interactions, which are associated with source-term bilinears appearing in Eq. (13) [11]. Hereby, SC and AFM denote superconductivity and antiferromagnetism, respectively. In addition, chiral SC1 and chiral SC2 are adopted to characterize two distinct sorts of chiral superconducting states.

Order parameters	Vertex matrixes of fermionic bilinears	Potential phases
Δ_1^c	$\mathcal{M}_1^c = \tau_0 \otimes \sigma_0$	charge instability
Δ_2^c	$\mathcal{M}_2^c = \tau_0 \otimes \sigma_1$	x -current
Δ_3^c	$\mathcal{M}_3^c = \tau_0 \otimes \sigma_2$	bond density
Δ_4^c	$\mathcal{M}_4^c = \tau_0 \otimes \sigma_3$	charge density wave
$\vec{\Delta}_1^s$	$\vec{\mathcal{M}}_1^s = \vec{\tau} \otimes \sigma_0$	Ferromagnet
$\vec{\Delta}_2^s$	$\vec{\mathcal{M}}_2^s = \vec{\tau} \otimes \sigma_1$	x -spin-current
$\vec{\Delta}_3^s$	$\vec{\mathcal{M}}_3^s = \vec{\tau} \otimes \sigma_2$	spin bond density
$\vec{\Delta}_4^s$	$\vec{\mathcal{M}}_4^s = \vec{\tau} \otimes \sigma_3$	AFM
Δ_1^{PP}	$\mathcal{M}_1^{\text{PP}} = \tau_2 \otimes \sigma_3$	s-wave SC
Δ_2^{PP}	$\mathcal{M}_2^{\text{PP}} = \tau_2 \otimes \sigma_1$	chiral SC1
Δ_3^{PP}	$\mathcal{M}_3^{\text{PP}} = \tau_2 \otimes \sigma_0$	chiral SC2
Δ_4^{PP}	$\mathcal{M}_4^{\text{PP}} = \tau_{0,1,3} \otimes \sigma_2$	triplet SC

II-Region. Under these respects, Table I consists of only one point for both Type-I-RFP and Type-III-RFP as well as three typical points for Type-II-RFP with considering the tendency of Type-II-Region in Fig. 4.

To be concrete, Fig. 3(a) indicates that, at Type-I-RFP, the parameters $\lambda_{00}/\lambda_{30}$, $\lambda_{01}/\lambda_{30}$, and $\lambda_{03}/\lambda_{30}$ flow divergently along the negative direction. In particular, the absolute strengths of $\lambda_{03}/\lambda_{30}$ and $\lambda_{00}/\lambda_{30}$ are the strongest and weakest. However, $\lambda_{13}/\lambda_{30}$, $\lambda_{20}/\lambda_{30}$, and $\lambda_{21}/\lambda_{30}$ are sign-unchanged during the whole RG process. Compared to Type-I-RFP, $\lambda_{01}/\lambda_{30}$ and $\lambda_{21}/\lambda_{30}$ at Type-III-RFP evolve towards zero. Additionally, Fig. 3(b) shows that $\lambda_{00}/\lambda_{30}$ and $\lambda_{03}/\lambda_{30}$ are driven to be equal but opposite to $\lambda_{20}/\lambda_{30}$ and $\lambda_{13}/\lambda_{30}$ in the lowest-energy limit. As for Type-II-RFP, interaction parameters delineated in Fig. 3(c)-(e) share the same sign-change (unchange) information with Type-I-RFP. In a sharp contrast to the other two types, it is of remarkable importance to emphasize that interaction parameters in the Type-II-Region approximately increase or decrease monotonically with the increase of η except some critical point. In addition to the difference of their concrete values, it is worth pointing out that the critical energy scales, at which RFPs are accessed, are nearly constants in Type-I-Region but instead proportional to η in both Type-II-Region and Type-III-Region.

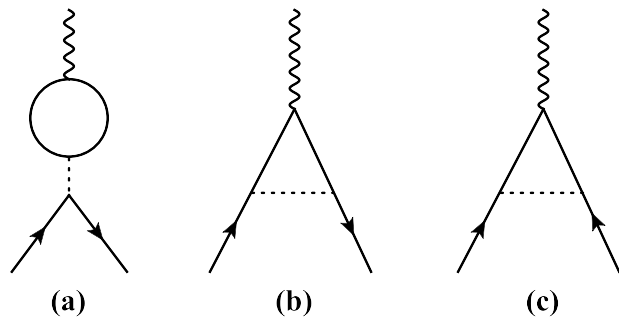


FIG. 6: One-loop corrections to the bilinear fermion-source terms [48, 51]: (a) and (b) represent the particle-hole channel and (c) specifies particle-particle channel. The solid, dash, and wave lines correspond to the fermion, fermion-fermion interaction and source term fields, respectively.

Before closing this section, it is necessary to present several comments on the flow tendencies of Fig. 2 and Fig. 3. Roughly speaking, there are two facets responsible for this issue. On one hand, the correlations among different sorts of fermionic interactions are less important and even negligible once the system is far enough away from the instability point. In comparison, both interactions and fluctuations play more important roles with accessing the instability point, yielding sensitive changes of interaction parameters. This indicates that the competition among all these distinct types of fermion-fermion interactions becomes stronger and stronger as the instability is approached, but instead weaker and weaker with deviating from that point. As a consequence, the RFP with strong couplings is a significant impetus to trigger a multitude of unusual phenomena including instabilities and critical physical behaviors [45, 48, 51, 81–88]. Stimulated by these, we are going to investigate the potential instabilities around three distinct types of RFPs in the upcoming section and defer the underlying critical physical behaviors to Sec. V.

IV. INSTABILITIES INDUCED BY FERMION-FERMION INTERACTIONS

With the variation of structural coefficient η , we have confirmed in previous section there exist three distinct types (regions) of RFPs attesting to the subtle fermion-fermion interactions. As mentioned previously, instabilities are tightly linked to these RFPs, which are well-known signatures of symmetry breaking [11, 47, 48, 51, 81–88, 105]. In this respect, it is of enormous interest to seek and identify the leading instability and its related phase transition.

In order to justify potential types of symmetry breaking, we are suggested to bring out the following source terms that collect both the charge and spin channels [11,

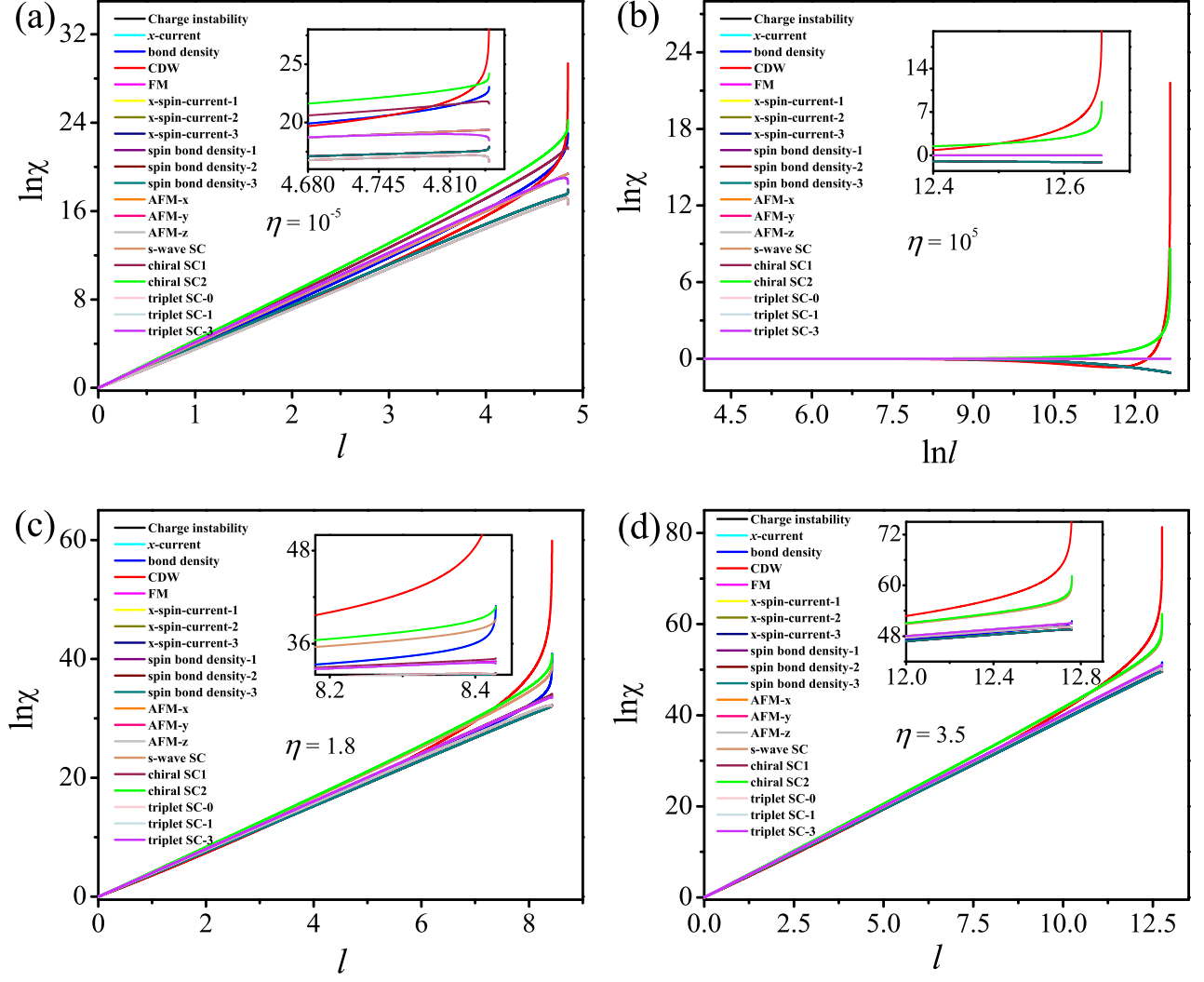


FIG. 7: (Color online) Flows of all particle-hole and particle-particle susceptibilities catalogued in Table II as functions of the RG evolution parameter l by approaching distinct types of RFPs classified and illustrated in Fig. 4 and Fig. 5. The x -spin-current- i and spin bond density- i with $i = 1, 2, 3$ as well as triplet SC- j with $j = 0, 1, 3$ and AFM- ζ with $\zeta = x, y, z$ are employed to specify distinct components of corresponding states as detailedly shown in Table II.

45, 48, 106]

$$\begin{aligned}
 S_{\text{soi}} = & \int d\tau \int d^2\mathbf{x} \sum_{i=1}^4 (\Delta_i^c \Psi^\dagger \mathcal{M}_i^c \Psi + \vec{\Delta}_i^s \cdot \Psi^\dagger \vec{\mathcal{M}}_i^s \Psi) \\
 & + \int d\tau \int d^2\mathbf{x} \sum_{i=1}^4 (\Delta_i^{\text{PP}} \Psi^\dagger \mathcal{M}_i^{\text{PP}} \Psi^* + \text{H.c.}) \quad (13)
 \end{aligned}$$

Hereby, the vertex matrixes $\mathcal{M}_i^{c/s}$ with $i = 1, 2, 3, 4$ denote various sorts of fermionic bilinears in the particle-hole part consisting of both charge and spin channels. In comparison, $\mathcal{M}_i^{\text{PP}}$ correspond to possible fermionic bilinears in the particle-particle situation [45, 48]. In addition, the couplings $\Delta_i^{c/s}$ and Δ_i^{PP} serve as the strengths of associated fermion-source terms, which can be regarded as

order parameters accompanied by corresponding symmetry breakings. In principle, the onset of fermionic bilinear is a manifest signal for certain instability and hence implies a phase transition tied to some symmetry breaking [47, 81, 84, 85, 105, 107]. Table II catalog the primary candidates of fermion bilinears and related phase transitions for our system.

A question is then naturally raised, which instability is the dominant one around three different types of RFPs. To elucidate this, we need to add the source terms (13) into our effective model. In this sense, the parameters Δ_i are entangled with the fermion-fermion interactions after taking into account one-loop fermion-fermion corrections as diagrammatically illustrated in Fig. 6. After carrying out analogous procedures in Sec. II B [45, 48], we notice that the strength of source term would be sen-

sitive to energy scales and subject to the following set of RG evolutions

$$\frac{d\Delta_i^{c/s,PP}}{dl} = \mathcal{G}_i^{c/s,PP} \Delta_i^{c/s,PP}, \quad (14)$$

where the index i runs from 1 to 4 and the coefficients $\mathcal{G}_i^{c/s,PP}$ are closely dependent upon the fermion-fermion interactions plus structural parameters d_1 and d_3 . The details for the flows of source terms and coefficients $\mathcal{G}_i^{c/s,PP}$ are stored in Appendix C.

To proceed, we are capable of capturing the corresponding susceptibilities around the RFPs by adopting the relationship [45, 48]

$$\delta\chi = -\frac{\partial^2 \delta f}{\partial \Delta(0) \partial \Delta^*(0)}, \quad (15)$$

with f being the free energy density. Concerning the ground state can be characterized by the susceptibility with the strongest divergence [11, 47, 48, 51, 81–88, 105, 108], we are now in a suitable position to identify the very dominant instability and the associated phase transition nearby the corresponding RFP by computing and comparing the susceptibilities of all underlying instabilities listed in Table II.

To this end, we are forced to combine the RG evolutions of fermion-fermion interactions (12) and energy-dependent strengths of source terms (14) in conjunction with the connections between susceptibilities and source-term couplings (15). After implementing long but straightforward numerical analysis, we are eventually left with the energy-dependent susceptibilities of all potential instabilities, which carry the low-energy physical information and determine the fates of all sorts of possible instabilities nearby distinct types of RFPs as apparently displayed in Fig. 7.

Subsequently, we deliver the primary results covered in Fig. 7. At the first sight, we figure out that all kinds of susceptibilities are fairly susceptible to energy scales and climb up quickly with accessing any sorts of the potential RFPs. Especially, it is of peculiar interest to address that fermion-fermion interactions are rather in favor of charge density wave (CDW). On one hand, the CDW susceptibility manifestly dominates over all other types once the system is tuned towards the expected RFP. On the other, this result is qualitatively insensitive to η . In other words, this kind of susceptibility is inevitable to be the strongest one no matter which type (region) of RFP is approached. Consequently, we come to a conclusion schematically illustrated in Fig. 8 that the leading instability is directly associated with a phase transition from QBCP semimetal to CDW state under the influence of fermion-fermion couplings in the 2D QBCP materials sited on the kagomé lattice without time-reversal symmetry. Compared to the traditional Peierls instability activated by the spontaneous symmetry breaking of ground state [109], this CDW instability essentially originates from the dynamical spontaneous symmetry breaking which is generated

by the particle-hole condensations owing to marginally relevant fermion-fermion interactions in the low-energy regime. It is worth pointing out that this result is basically in agreement with recent works on analogous compounds [110–113]. This suggests that the CDW state is another winner driven by fermion-fermion interactions in the 2D QBCP materials besides quantum anomalous Hall and quantum spin Hall states in its checkerboard-lattice counterpart with time-reversal symmetry [48, 51].

Next, we move to consider the subleading instabilities. Unlike the leading instability, we learning from Fig. 7 find that the subleading instabilities are of close relevance to the structural coefficient η and exhibit diverse fates in the vicinity of three different types of RFPs. To be concrete, as depicted in Fig. 7(a), susceptibilities of x -current, bond density, and chiral SC-2 are increased and become subdominant nearby Type-I-RFP. With respect to Type-II-RFP, the tendencies of all instabilities share the basic fates with Type-I-RFP once η is small. However, while η is increased to 1.8, the susceptibility of s-wave SC illustrated in Fig. 7(c) becomes comparable with that of x -current, bond density, and chiral SC-2 and thus can be regarded as another subleading instability. Further, s-wave SC and chiral SC-2 are gradually enhanced with the continue increase of η as delineated in Fig. 7(d) and become only two subdominant ones via eliminating x -current and bond density at $\eta = 3.5$. As for Type-III-RFP, Fig. 7(b) indicates that the qualitative results are analogous to Type-II-RFP's at $\eta = 3.5$, namely s-wave SC and chiral SC-2 are subleading phases. At last, it is notable to highlight that the critical energy scale (E_c) is rapidly decreased (i.e. l_c is rapidly increased) with tuning up the value of η . This means that an enhancement of η is harmful to the emergence of instability.

To be brief, the dominant instability driven by fermion-fermion interactions is always tied to the CDW state irrespective of the value of η . In contrast, there exist four η -dependent candidates including the x -current and bond density as well as chiral SC-2 plus s-wave SC that are subordinate to the CDW state. Especially, we realize that the chiral SC-2 state is always subleading irrespective of concrete value of η . Rather, both the x -current and bond density can only play a subdominant role at a weak η . As the η is progressively increased, they share the positions with and eventually are replaced by the s-wave SC. Albeit the dominant instability generally takes a major responsibility for the low-energy physics, these subdominant ones might be in charge of related phenomena while the system is impacted by unexpected facets. For the sake of completeness, we are about to investigate how the behaviors of physical quantities are affected by the leading instability in the forthcoming section.

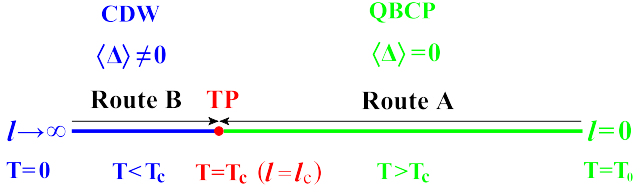


FIG. 8: (Color online) Schematic diagram for temperature-tuned phase transition from a 2D QBCP semimetal to a CDW state. The T_c and “TP” designate the critical temperature and the transition point (or critical point) associated with the CDW instability, respectively. Route A and Route B exhibit two distinct paths to access the critical point (despite T_c ($T_c \gtrsim 0$) is very small as l_c is a relatively bigger value as shown in Fig. 2, it hereby is enlarged to make a sharp contrast).

V. CRITICAL PHYSICAL IMPLICATIONS

On the basis of intimate fermion-fermion interactions in the low-energy sector, we have presented potential instabilities induced by fermionic interactions and corroborated in Sec. IV a direct connection between the overarching instability and CDW phase transition at certain RFP. At this stage, the RFP is tantamount to a phase transition point, at which the fluctuations are always so ferocious that usually render a plenty of singular critical behaviors [90, 114–119]. Accordingly, it is interesting to investigate possible physical implications triggered by the onset of CDW state.

For this purpose, it is necessary to clarify the overall scenario of our basic results sketched in Fig. 8. It consists of two subspaces separated by the critical point with $l = l_c$ ($T = T_c$) corresponding to a disordered QBCP semimetal state located at the region $(T_c, T_0]$ and an ordered CDW state at $T < T_c$, respectively. Obviously, there exist two routes that are Route A starting from the disordered phase (QBCP) and Route B from the ordered phase (CDW) to access the phase transition point (TP). In principle, one can either go along Route A or Route B to track the effects of phase transition on the

physical observables. However, it is insensible to probe into the physical behaviors as it approaches the critical point through Route B since the RG approach is strictly based upon the perturbative theory. In this respect, we within this section go along with Route A to tentatively investigate the physical observables on the right side of critical point with $T > T_c$. Given that the band structure and dispersion of the QBCP system are stable in region $T > T_c$, but destroyed at $T < T_c$, this strategy at least can provide a preliminary understanding of criticality nearby CDW instability.

Technically, it seems inappropriate to capture the effects of CDW instability for the region $T > T_c$ since the average value of order parameter Δ vanishes at $T > T_c$ as illustrated in Fig. 8. However, it is worth pointing out the fluctuation of order parameter is nonzero albeit $\langle \Delta \rangle = 0$, and becomes stronger and stronger as the critical point is approached along with Route A, eventually diverges at the critical point. In this sense, we are suggested to regard Δ as a fluctuation of CDW order parameter, which is generated by the fermion-fermion interactions, to collect the influences of CDW instability, and then examine how the physical quantities vary by adjusting the value of Δ (it is equivalent to approaching the TP along with Route A). To this end, we introduce a constant Δ to represent the fluctuation associated with the leading stability and add it by hand into the fermionic free propagator of the 2D QBCP system [72]. Then the free fermionic propagator (7) dressed by one-loop corrections is thus recast as

$$G_0(i\omega_n, \mathbf{k}) = \left(-i\omega_n + (d_3 \mathbf{k}^2 + \Delta) \Sigma_{03} + d_1 \Sigma_{01} (k_x^2 - k_y^2) + d_2 \Sigma_{02} k_x k_y \right)^{-1}, \quad (16)$$

where $\omega_n = (2n + 1)\pi T$ with n being an integer stands for the Matsubara frequency. To proceed, performing analytical continuation $i\omega_n \rightarrow \omega_n + i\delta$, we are subsequently left with the retarded fermion propagator as follows [119],

$$G_0^{\text{ret}}(\omega_n, \mathbf{k}) = \frac{(\omega_n + i\delta) + (d_3 k^2 + \Delta) \Sigma_{03} + d_1 k^2 (\cos 2\theta \Sigma_{01} + \sin 2\theta \Sigma_{02})}{(-\omega_n^2 - 2i\omega_n \delta + d_3^2 k^4 + 2d_3 k^2 \Delta + \Delta^2 + d_1^2 k^4)}. \quad (17)$$

It is now in a suitable position to extract the qualitative effects sparked by the formation of order parameter on the physical quantities. Without loss of generality, we within this section put our focus on the density of states (DOS) as well as specific heat and compressibility of quasiparticles.

A. DOS

At first, let us concentrate on the DOS under the influence of CDW fluctuation with approaching the critical point through Route A. To achieve this goal, one necessitates the corresponding spectral function, which is directly connected to the retarded fermion propaga-

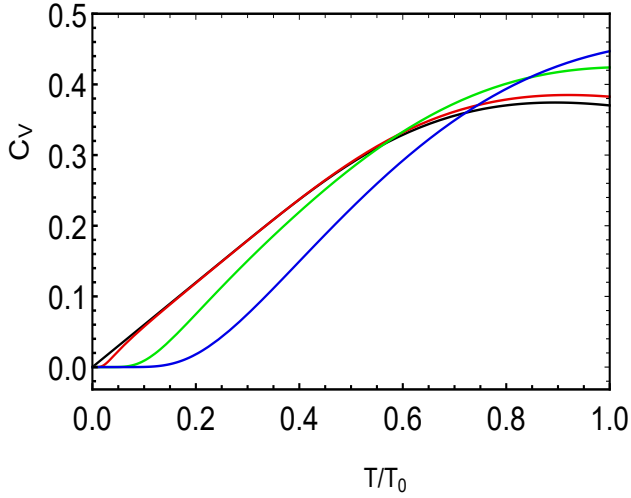


FIG. 9: (Color online) Temperature dependence of the specific heat C_V accessing the Type-II-RFP under the CDW fluctuation. The black, red, green, and blue lines correspond to $\Delta' = 0$, $\Delta' = 0.1$, $\Delta' = 0.5$, and $\Delta' = 1$, respectively (the qualitative results for Type-I-RFP are analogous and hence not shown here).

tor (17) [89, 119] and of the following form

$$\begin{aligned} & \mathcal{A}(\omega_n, \mathbf{k}) \\ &= -\frac{1}{\pi} \text{Tr} (\text{Im} G_0^{\text{ret}}(\omega_n, \mathbf{k})) \\ &= 4N |\omega_n| \delta(d_3^2 k^4 + 2d_3 k^2 \Delta + \Delta^2 + d_1^2 k^4 - \omega_n^2), \end{aligned} \quad (18)$$

where the number N characterizes the fermion flavor. With this respect, the DOS of quasiparticles consequently can be cast as

$$\rho(\omega_n) = N \int_0^{\Lambda_0} \int_0^{2\pi} \frac{k dk d\theta}{(2\pi)^2} \mathcal{A}(\omega_n, \mathbf{k}). \quad (19)$$

Prior to inspecting the impact of order parameter, it is necessary to briefly discuss the circumstance in the absence of instability. Removing the fluctuation via taking $\Delta \rightarrow 0$ limit in Eq. (19) directly gives rise to

$$\rho(\omega_n) = \frac{N}{2\pi \sqrt{d_3^2 + d_1^2}}. \quad (20)$$

This is in reminiscence of the fact that the DOS of 2D

QBCP system is a finite constant at the Fermi surface [44, 48].

Subsequently, we go to examine the very influence of CDW fluctuation. Based upon the general result (19) in tandem with the essential properties of δ function, we notice that the DOS would be broken down into two distinct situations depending upon Δ 's magnitude. On one hand, one can find the ω_n or temperature (T) dependence of DOS at $|\Delta| < T$ is rewritten as follows

$$\rho(\omega_n) = \frac{N}{2\pi \sqrt{d_3^2 + d_1^2 (1 - \frac{\Delta^2}{\omega_n^2})}}. \quad (21)$$

On the other hand, a large order parameter with $|\Delta| > T$ is of particular detriment to DOS which disappears exactly at the instability, namely

$$\rho(\omega_n) = 0. \quad (22)$$

These manifestly shed light on the important role of CDW fluctuation in the proximity of instability. Compared to a finite DOS for 2D QBCP materials with $\Delta = 0$, we figure out that it nearby Fermi surface (QBCP) is slightly enhanced while the system is a little far away from instability with $|\Delta| < T$. In addition, its concrete values as clearly designated in Eqs. (20)-(21) are heavily dependent upon two microscopic parameters d_3 and d_1 , which are closely associated with different types of RFPs. However, once the RFP is sufficiently approached with $|\Delta| > T$, the onset of large order parameter substantially suppresses the DOS due to ferocious fluctuations. In other words, the band structure of 2D QBCP systems would be completely sabotaged [52, 82]. It is worth emphasizing that we have checked all sorts of RFPs share the analogous qualitative results.

B. Specific heat

Next, we are going to shift our target to the specific heat of quasiparticles. For the sake of completeness, we hereby bring out an infinitesimal chemical potential μ into our effective theory [89, 120]. As a result, the corresponding free fermionic propagator in the Matsubara formalism is reformulated as

$$G_0(i\omega_n, \mathbf{k}) = \frac{1}{i\omega_n + \mu - \mathcal{H}_0(k) - \Delta \Sigma_{03}} = -\frac{i\omega_n + \mu + (d_3 k^2 + \Delta) \Sigma_{03} + d_1 \Sigma_{01} k^2 \cos 2\theta + d_1 \Sigma_{02} k^2 \sin 2\theta}{(\omega_n - i\mu)^2 + (d_3 k^2 + \Delta)^2 + d_1^2 k^4}. \quad (23)$$

Following the tactic in Ref. [89], we integrate over all frequencies and then write the free energy of the fermions

as

$$f(T, \mu) = -2N \sum_{\alpha \pm 1} \int \frac{d^2 \mathbf{k}}{(2\pi)^2} \left[\epsilon(\mathbf{k}) + T \ln \left(1 + e^{-\frac{\epsilon(\mathbf{k}) + \alpha \mu}{T}} \right) \right], \quad (24)$$

where the energy is designated as

$$\epsilon(\mathbf{k}) \equiv \sqrt{(d_3 \mathbf{k}^2 + \Delta)^2 + d_1^2 \mathbf{k}^4}. \quad (25)$$

To simplify our study, we take advantage of transformation $f(T) - f(0) \rightarrow f(T)$ to eliminate the zero-point energy and obtain a compact free energy as follows

$$f(T, \mu) = -2NT \sum_{\alpha \pm 1} \int_0^{\Lambda_0} \int_0^{2\pi} \frac{kdkd\theta}{(2\pi)^2} \ln \left(1 + e^{-\frac{\epsilon(\mathbf{k}) + \alpha\mu}{T}} \right). \quad (26)$$

In this sense, we hereafter only pour our attention into $\mu = 0$ situation for specific heat, which is based upon two points. On one side, the starting point (6) is restricted to zero chemical potential at the QBCP. On the other side, this work only concerns qualitative phenomena of physical implications triggered by an instability irrespective of the value of μ . To proceed, supposing $\mu = 0$ in Eq. (26) gives rise to

$$f(T) = -4NT \int_0^{\Lambda_0} \int_0^{2\pi} \frac{kdkd\theta}{(2\pi)^2} \ln \left(1 + e^{-\frac{\epsilon(\mathbf{k})}{T}} \right). \quad (27)$$

Taking the derivatives of free energy with respect to temperature forthrightly yields to the specific heat (C_V) [89, 120]

$$C_V(T) = -T \frac{\partial^2 f(T)}{\partial T^2} = \frac{2N}{\pi T^2} \int_0^{\Lambda_0} \frac{kdk \epsilon^2(\mathbf{k}) e^{-\frac{\epsilon(\mathbf{k})}{T}}}{\left(e^{-\frac{\epsilon(\mathbf{k})}{T}} + 1 \right)^2}. \quad (28)$$

$$C_V(T) = \frac{2NT_0^{\frac{3}{2}}}{\pi\sqrt{T}} \frac{\left[6 \frac{(d_3^2 + d_1^2)}{(T/T_0)^2} \frac{e^{-\frac{\sqrt{d_3^2 + d_1^2}}{T/T_0}}}{1 + e^{-\frac{\sqrt{d_3^2 + d_1^2}}{T/T_0}}} - 12 \frac{\sqrt{d_3^2 + d_1^2}}{T/T_0} \log \left(1 + e^{-\frac{\sqrt{d_3^2 + d_1^2}}{T/T_0}} \right) - 12 \text{Li}_2 \left(-e^{-\frac{\sqrt{d_3^2 + d_1^2}}{T/T_0}} \right) - \pi^2 \right]}{12(d_3^2 + d_1^2)^{\frac{1}{2}}}, \quad (31)$$

with $\text{Li}_2(z)$ corresponding to a polylogarithmic function [121]. This will be utilized to compare with its $\Delta' \neq 0$ counterparts.

Subsequently, we endeavor to investigate the nontrivial situation with a moderate order parameter once the system is adjacent to RFP (not exactly accessed). Carrying out the numerical analysis of Eqs. (29) and (31) yields several interesting features shown in Fig. 9 and Fig. 10. Studying from Fig. 9, one broadly realizes that the fates of $C_V(T)$ around Type-II-RFP are fairly dependent upon Δ' (the qualitative result for Type-I-RFP is analogous and thus not shown here). In the low-temperature region, the order parameter apparently hampers the specific heat. On the contrary, C_V gains a slight lift in the high-temperature region. In comparison, Fig. 10 displays that Δ' always brings some detriments to C_V as the system is close to the Type-III-RFP. In particular, CDW instability drives the specific heat $C_V(T) \rightarrow 0$ as

In order to facilitate our calculations, it is convenient to rescale the momentum and order parameter with the cutoff temperature T_0 that is related to the cutoff Λ_0 by $T_0 \equiv \Lambda_0^2$, namely $k' \equiv k/\sqrt{T_0}$ and $\Delta' \equiv \Delta/T_0$ [89]. As a corollary, we can convert the $C_V(T)$ into the following form

$$C_V(T) = \frac{2NT_0^3}{\pi T^2} \int_0^1 \frac{k' dk' \epsilon'^2(\mathbf{k}', \Delta') e^{-\frac{\epsilon'(\mathbf{k}', \Delta')}{T/T_0}}}{\left(e^{-\frac{\epsilon'(\mathbf{k}', \Delta')}{T/T_0}} + 1 \right)^2}, \quad (29)$$

where the ϵ' is designated as

$$\epsilon'(\mathbf{k}', \Delta') \equiv \sqrt{(d_3 k'^2 + \Delta')^2 + d_1^2 k'^4}. \quad (30)$$

On the basis of the general expression for $C_V(T)$ (29), a few comments on the specific heat are addressed under the fluctuation of an order parameter kindled by the CDW instability. We at first tackle the limit case with $\Delta' = 0$ (i.e., the 2D QBCP state). In this circumstance, it is fortunate that the analytical result (29) can be obtained by integrating out the momenta

$T \rightarrow T_c$, which is a finite constant in the absence of fluctuation. Eventually, we examine the limit $\Delta' \gg 1$ (namely $\Delta \gg T_0$), which would be ignited once the RFP is approached. In this respect, combining Eq. (29) with this limit is expected to grasp the central point of specific heat

$$C_V(T) \approx \frac{NT_0^3 \Delta'^2}{\pi T^2 e^{\frac{\Delta'}{T/T_0}}}, \quad (32)$$

which signals $\lim_{\Delta' \rightarrow \infty} C_V(T) \rightarrow 0$. It manifestly indicates that C_V is profoundly reduced by the strong fluctuation of order parameter at the CDW instability.

C. Compressibility

At last, with the help of temperature- and μ -dependent free energy derived in Eq. (26), we are allowed to verify

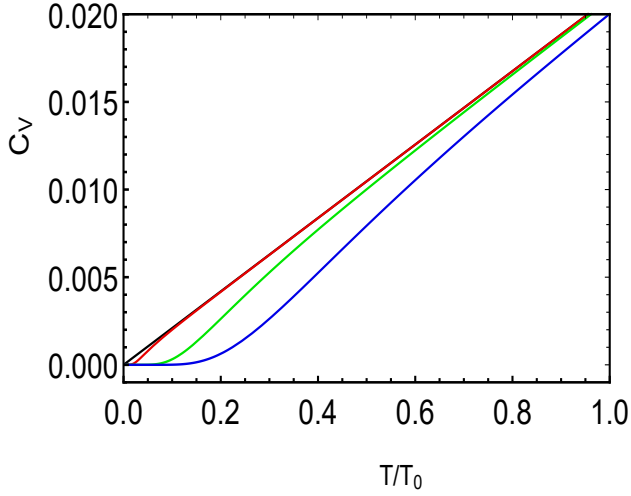


FIG. 10: (Color online) Temperature dependence of the specific heat C_V approaching the Type-III-RFP under the CDW fluctuation. The black, red, green, and blue lines correspond to $\Delta' = 0$, $\Delta' = 0.1$, $\Delta' = 0.5$, and $\Delta' = 1$, respectively.

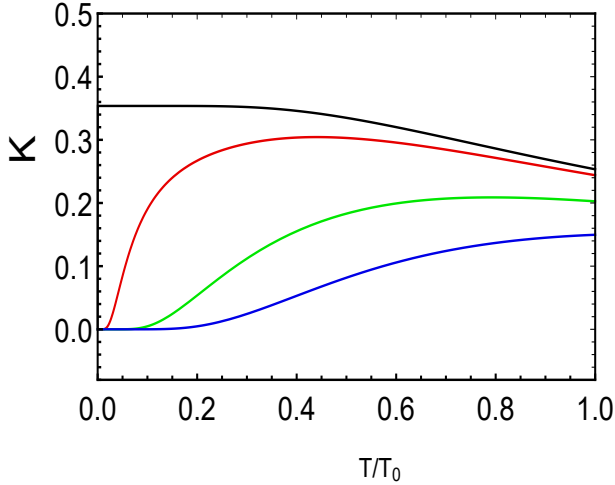


FIG. 11: (Color online) Temperature dependence of the compressibility κ approaching the Type-II-RFP under the CDW fluctuation. The black, red, green, and blue lines correspond to $\Delta' = 0$, $\Delta' = 0.1$, $\Delta' = 0.5$, and $\Delta' = 1$, respectively (the basic conclusions for both Type-I-RFP and Type-III-RFP are similar and hence not shown here).

how the compressibility of quasiparticles labeled by κ behaves in the proximity of the leading instability. Concretely, the temperature dependence of κ reads [89, 122–124]

$$\kappa(T) = - \left. \frac{\partial^2 f(T, \mu)}{\partial \mu^2} \right|_{\mu=0} = \frac{2N}{\pi T} \int_0^{\Lambda_0} k dk \frac{e^{-\frac{\epsilon(\mathbf{k})}{T}}}{\left(e^{-\frac{\epsilon(\mathbf{k})}{T}} + 1 \right)^2}, \quad (33)$$

with $\epsilon(\mathbf{k})$ being denominated in Eq. (25) for the absence of chemical potential. We then adopt the same rescalings

employed in Sec. VB and are left with

$$\kappa(T) = \frac{2N}{\pi(T/T_0)} \int_0^1 k' dk' \frac{e^{-\frac{\epsilon'(\mathbf{k}', \Delta')}{T/T_0}}}{\left(e^{-\frac{\epsilon'(\mathbf{k}', \Delta')}{T/T_0}} + 1 \right)^2}, \quad (34)$$

where $\epsilon'(\mathbf{k}', \Delta')$ is designated in Eq. (30).

Accordingly, the analytical expressions for $\Delta' = 0$ and $\Delta' \gg 1$ can also be easily obtained,

$$\kappa(T, \Delta' = 0) = \frac{N \tanh\left(\frac{\sqrt{d_3^2 + d_1^2}}{2(T/T_0)}\right)}{2\pi\sqrt{d_3^2 + d_1^2}}, \quad (35)$$

$$\kappa(T, \Delta' \gg 1) \approx \frac{N}{\pi(T/T_0)} e^{-\frac{\Delta'}{T/T_0}}. \quad (36)$$

Numerically implementing Eq. (34) leads to Fig. 11, which implies that the compressibility is severely suppressed by a finite order parameter. Additionally, Eq. (36) proposes that the compressibility goes toward vanishment because of the divergent fluctuation of order parameter exactly at the RFP. It is worth emphasizing that all these basic conclusions are insensitive to concrete values of RFP. In such circumstance, this phenomenon can be regarded as the third critical behavior driven by fermion-fermion interactions [82, 89].

To recapitulate, the primary task of this work is to judge whether and which kind of phase transition can be induced by the fermion-fermion interactions, which, to a large extent, is basically finished in Sec. III and Sec. IV. In comparison, the physical behaviors around the critical point are only our secondary concerns. Although the strategy employed in this section may be not the best one, we are able to qualitatively capture the behaviors of these physical quantities via regarding the parameter Δ as a fluctuation and tuning the variation of Δ to simulate the access of critical point along with Route A illustrated in Fig. 8.

VI. SUMMARY

In summary, we attentively verify how the low-energy properties of 2D spin-1/2 QBCP fermionic systems on the kagomé lattice are impacted by all sixteen sorts of marginal fermion-fermion interactions. For the purpose of treating these degrees of freedom on the same footing, we resort to the momentum-shell RG method [78–80], which is a well-trodden strategy for the description of hierarchical physics under the coexistence of multiple sorts of interactions. In the spirit of standard RG analysis, a set of coupled flow equations of all interaction strengths are derived by taking into account one-loop corrections of the correlated Feynman diagrams. After vigilantly analyzing these RG evolutions, several physical properties

ignited by marginally relevant fermion-fermion interactions are addressed in the low-energy sector.

At first, we notice that some sorts of fermion-fermion couplings coalesce with the decrease of energy scale due to their intimate correlations. This tenders just six of them can flow independently and evolve divergently with lowering energy scales. In this respect, we only need to contemplate the energy-dependent trajectories of six non-trivial fermionic couplings. In order to work in the perturbative theory, it is convenient to rescale these strong-coupling interactions with a non-sign changed parameters (such as λ_{30}) and obtain the relative flows of interaction parameters as well as their RFPs that directly govern the critical physics [45, 48, 51]. In particular, these RFPs are of close association with the coefficient composed by two structure parameters (i.e., $\eta \equiv d_3/d_1$). To be concrete, Fig. 4 and Fig. 5 unambiguously manifest three qualitatively distinct η -dependent regions, which are named as Type-I-Region, Type-II-Region, and Type-III-Region residing in $\eta < C_1$, $C_1 < \eta < C_2$, and $\eta > C_2$, respectively. Focusing on the vicinity of RFPs in these three different regions, we then carefully investigate the underlying instabilities, which are accompanied by corresponding symmetry breakings and tied to related phase transitions [47, 48, 51, 81–88]. On the basis of numerical RG studies together with comparisons of susceptibilities, we, reading off Fig. 7, draw a conclusion that the CDW instability is always dominant over all other candidates irrespective of the specific value of η . In contrast, four subleading ones are also manifestly proposed, which include x -current, bond density, chiral SC-2, and s -wave SC depending upon the variation of η . Furthermore, as the leading instability is accessed along with Route A shown in Fig. 8, we tentatively examine the effects of fluctuation induced by the phase transition from a QBCP semimetal to CDW state on physical implications consisting of DOS and specific heat as well as compressibility. To be specific, the development of CDW state is very harmful to these three kinds of physical observables. Especially, they are all considerably suppressed and even

vanish once the fluctuation of order parameter is strong enough in the vicinity of CDW instability. These results are reminiscent of quantum critical behaviors in the low-energy regime [90, 114–119].

We wish these studies would supplement current understandings of 2D QBCP semimetals and open helpful routes to promote further research of 2D QBCP materials as well as explore their cousin materials in the future.

ACKNOWLEDGEMENTS

J.W. is partially supported by the National Natural Science Foundation of China under Grant No. 11504360. The authors would like to thank Jie-Qiong Li, Xiao-Yue Ren, and Yao-Ming Dong for helpful discussions.

AUTHOR CONTRIBUTIONS

J. W. initiated and supervised the project as well as performed the numerical analysis and wrote the manuscript. Y.H.Z carried out the analytical calculations and plotted figures.

ADDITIONAL INFORMATION

Competing interests: The authors declare no Competing Financial or Non-Financial Interests.

Appendix A: One-loop corrections

The one-loop corrections to self-energy and fermion-fermion interactions are depicted in Fig. 12. After long but straightforward calculations, we obtain [48, 51]

$$\begin{aligned}
S_{00} = & - \int_{-\infty}^{\infty} \frac{d\omega_1 d\omega_2 d\omega_3}{(2\pi)^3} \int \frac{d^2\mathbf{k}_1 d^2\mathbf{k}_2 d^2\mathbf{k}_3}{(2\pi)^6} \Psi^\dagger(\omega_1, \mathbf{k}_1) \Sigma_{00} \Psi(\omega_2, \mathbf{k}_2) \Psi^\dagger(\omega_3, \mathbf{k}_3) \Sigma_{00} \Psi(\omega_1 + \omega_2 - \omega_3, \mathbf{k}_1 + \mathbf{k}_2 - \mathbf{k}_3) \\
& \times [2d_3^2(\lambda_{00}\lambda_{03} + \lambda_{10}\lambda_{13} + \lambda_{20}\lambda_{23} + \lambda_{30}\lambda_{33}) + d_1^2(\lambda_{00}\lambda_{01} + \lambda_{10}\lambda_{11} + \lambda_{20}\lambda_{21} + \lambda_{30}\lambda_{31} + \lambda_{00}\lambda_{02} + \lambda_{10}\lambda_{12} + \lambda_{20}\lambda_{22} \\
& + \lambda_{30}\lambda_{32})] \frac{l}{4\pi(d_3^2 + d_1^2)^{\frac{3}{2}}}, \tag{A1}
\end{aligned}$$

$$\begin{aligned}
S_{10} = & \int_{-\infty}^{\infty} \frac{d\omega_1 d\omega_2 d\omega_3}{(2\pi)^3} \int \frac{d^2\mathbf{k}_1 d^2\mathbf{k}_2 d^2\mathbf{k}_3}{(2\pi)^6} \Psi^\dagger(\omega_1, \mathbf{k}_1) \Sigma_{10} \Psi(\omega_2, \mathbf{k}_2) \Psi^\dagger(\omega_3, \mathbf{k}_3) \Sigma_{10} \Psi(\omega_1 + \omega_2 - \omega_3, \mathbf{k}_1 + \mathbf{k}_2 - \mathbf{k}_3) \\
& \times \{2d_3^2[\lambda_{20}\lambda_{30} + \lambda_{21}\lambda_{31} + \lambda_{22}\lambda_{32} + \lambda_{23}\lambda_{33} - (\lambda_{13}\lambda_{00} + \lambda_{10}\lambda_{03} + \lambda_{21}\lambda_{32} + \lambda_{22}\lambda_{31})] + d_1^2[2(\lambda_{20}\lambda_{30} + \lambda_{21}\lambda_{31} \\
& + \lambda_{22}\lambda_{32} + \lambda_{23}\lambda_{33}) - (\lambda_{01}\lambda_{10} + \lambda_{00}\lambda_{11} + \lambda_{22}\lambda_{33} + \lambda_{23}\lambda_{32} + \lambda_{12}\lambda_{00} + \lambda_{10}\lambda_{02} + \lambda_{23}\lambda_{31} + \lambda_{21}\lambda_{33})]\} \frac{l}{4\pi(d_3^2 + d_1^2)^{\frac{3}{2}}}, \tag{A2}
\end{aligned}$$

$$S_{20} = \int_{-\infty}^{\infty} \frac{d\omega_1 d\omega_2 d\omega_3}{(2\pi)^3} \int \frac{d^2\mathbf{k}_1 d^2\mathbf{k}_2 d^2\mathbf{k}_3}{(2\pi)^6} \Psi^\dagger(\omega_1, \mathbf{k}_1) \Sigma_{20} \Psi(\omega_2, \mathbf{k}_2) \Psi^\dagger(\omega_3, \mathbf{k}_3) \Sigma_{20} \Psi(\omega_1 + \omega_2 - \omega_3, \mathbf{k}_1 + \mathbf{k}_2 - \mathbf{k}_3)$$

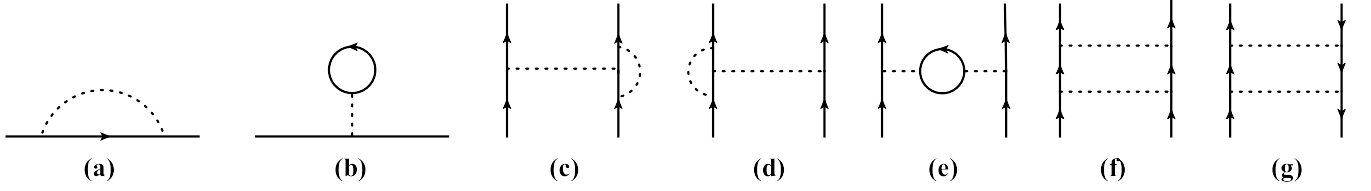


FIG. 12: One-loop corrections to (a)-(b): the fermion propagator and (c)-(g): the fermion-fermion interactions. The solid and dashed lines characterize the fermion propagator and four-fermion interactions, respectively [48, 51].

$$\begin{aligned}
S_{33} = & \int_{-\infty}^{\infty} \frac{d\omega_1 d\omega_2 d\omega_3}{(2\pi)^3} \int \frac{d^2\mathbf{k}_1 d^2\mathbf{k}_2 d^2\mathbf{k}_3}{(2\pi)^6} \Psi^\dagger(\omega_1, \mathbf{k}_1) \Sigma_{33} \Psi(\omega_2, \mathbf{k}_2) \Psi^\dagger(\omega_3, \mathbf{k}_3) \Sigma_{33} \Psi(\omega_1 + \omega_2 - \omega_3, \mathbf{k}_1 + \mathbf{k}_2 - \mathbf{k}_3) \\
& \times \{2d_3^2[\lambda_{31}\lambda_{02} + \lambda_{32}\lambda_{01} + \lambda_{23}\lambda_{10} + \lambda_{20}\lambda_{13} - (\lambda_{30}\lambda_{00} + \lambda_{31}\lambda_{01} + \lambda_{32}\lambda_{02} + \lambda_{33}\lambda_{03})] + d_1^2[2(\lambda_{31}\lambda_{02} + \lambda_{32}\lambda_{01} \\
& + \lambda_{23}\lambda_{10} + \lambda_{20}\lambda_{13} + \lambda_{33}\lambda_{00} + \lambda_{33}\lambda_{03} + \lambda_{33}\lambda_{11} + \lambda_{33}\lambda_{12} + \lambda_{33}\lambda_{21} + \lambda_{33}\lambda_{22} + \lambda_{33}\lambda_{30}) - (\lambda_{32}\lambda_{00} + \lambda_{30}\lambda_{02} \\
& + \lambda_{23}\lambda_{11} + \lambda_{21}\lambda_{13} + \lambda_{31}\lambda_{00} + \lambda_{30}\lambda_{01} + \lambda_{22}\lambda_{13} + \lambda_{23}\lambda_{12}) - 2(\lambda_{33}\lambda_{01} + \lambda_{33}\lambda_{02} + \lambda_{33}\lambda_{10} + \lambda_{33}\lambda_{13} + \lambda_{33}\lambda_{20} \\
& + \lambda_{33}\lambda_{23} + \lambda_{33}\lambda_{31} + \lambda_{33}\lambda_{32} + 3\lambda_{33}\lambda_{33})]\} \frac{l}{4\pi(d_3^2 + d_1^2)^{\frac{3}{2}}}. \tag{A16}
\end{aligned}$$

Appendix B: RG flow equations of all interaction parameters

Combining our effective action (6) and the RG rescalings (8)-(11) as well as all the one-loop corrections presented in Appendix A, we consequently are left with the following coupled RG evolutions of fermion-fermion interactions after carrying out the standard procedures of RG analysis [48, 95, 97, 98]

$$\begin{aligned}
\frac{d\lambda_{00}}{dl} = & -\frac{1}{4\pi(d_3^2 + d_1^2)^{\frac{3}{2}}} [2d_3^2(\lambda_{00}\lambda_{03} + \lambda_{10}\lambda_{13} + \lambda_{20}\lambda_{23} + \lambda_{30}\lambda_{33}) + d_1^2(\lambda_{00}\lambda_{01} + \lambda_{10}\lambda_{11} + \lambda_{20}\lambda_{21} + \lambda_{30}\lambda_{31} \\
& + \lambda_{00}\lambda_{02} + \lambda_{10}\lambda_{12} + \lambda_{20}\lambda_{22} + \lambda_{30}\lambda_{32})], \tag{B1}
\end{aligned}$$

$$\begin{aligned}
\frac{d\lambda_{10}}{dl} = & \frac{1}{4\pi(d_3^2 + d_1^2)^{\frac{3}{2}}} \{2d_3^2[\lambda_{20}\lambda_{30} + \lambda_{21}\lambda_{31} + \lambda_{22}\lambda_{32} + \lambda_{23}\lambda_{33} - (\lambda_{13}\lambda_{00} + \lambda_{10}\lambda_{03} + \lambda_{21}\lambda_{32} + \lambda_{22}\lambda_{31})] \\
& + d_1^2[2(\lambda_{20}\lambda_{30} + \lambda_{21}\lambda_{31} + \lambda_{22}\lambda_{32} + \lambda_{23}\lambda_{33}) - (\lambda_{01}\lambda_{10} + \lambda_{00}\lambda_{11} + \lambda_{22}\lambda_{33} + \lambda_{23}\lambda_{32} + \lambda_{12}\lambda_{00} \\
& + \lambda_{10}\lambda_{02} + \lambda_{23}\lambda_{31} + \lambda_{21}\lambda_{33})]\}, \tag{B2}
\end{aligned}$$

$$\begin{aligned}
\frac{d\lambda_{20}}{dl} = & \frac{1}{4\pi(d_3^2 + d_1^2)^{\frac{3}{2}}} \{2d_3^2[\lambda_{30}\lambda_{10} + \lambda_{31}\lambda_{11} + \lambda_{32}\lambda_{12} + \lambda_{33}\lambda_{13} - (\lambda_{23}\lambda_{00} + \lambda_{20}\lambda_{03} + \lambda_{31}\lambda_{12} + \lambda_{32}\lambda_{11})] \\
& + d_1^2[2(\lambda_{30}\lambda_{10} + \lambda_{31}\lambda_{11} + \lambda_{32}\lambda_{12} + \lambda_{33}\lambda_{13}) - (\lambda_{21}\lambda_{00} + \lambda_{20}\lambda_{01} + \lambda_{32}\lambda_{13} + \lambda_{33}\lambda_{12} + \lambda_{22}\lambda_{00} \\
& + \lambda_{20}\lambda_{02} + \lambda_{33}\lambda_{11} + \lambda_{31}\lambda_{13})]\}, \tag{B3}
\end{aligned}$$

$$\begin{aligned}
\frac{d\lambda_{30}}{dl} = & \frac{1}{4\pi(d_3^2 + d_1^2)^{\frac{3}{2}}} \{2d_3^2[\lambda_{10}\lambda_{20} + \lambda_{11}\lambda_{21} + \lambda_{12}\lambda_{22} + \lambda_{13}\lambda_{23} - (\lambda_{33}\lambda_{00} + \lambda_{30}\lambda_{03} + \lambda_{11}\lambda_{22} + \lambda_{12}\lambda_{21})] \\
& + d_1^2[2(\lambda_{10}\lambda_{20} + \lambda_{11}\lambda_{21} + \lambda_{12}\lambda_{22} + \lambda_{13}\lambda_{23}) - (\lambda_{31}\lambda_{00} + \lambda_{30}\lambda_{01} + \lambda_{12}\lambda_{23} + \lambda_{13}\lambda_{22} + \lambda_{32}\lambda_{00} \\
& + \lambda_{30}\lambda_{02} + \lambda_{13}\lambda_{21} + \lambda_{11}\lambda_{23})]\}, \tag{B4}
\end{aligned}$$

$$\begin{aligned}
\frac{d\lambda_{01}}{dl} = & \frac{1}{8\pi(d_3^2 + d_1^2)^{\frac{3}{2}}} \{4d_3^2[\lambda_{01}\lambda_{00} + \lambda_{01}\lambda_{10} + \lambda_{01}\lambda_{11} + \lambda_{01}\lambda_{20} + \lambda_{01}\lambda_{21} + \lambda_{01}\lambda_{30} + \lambda_{01}\lambda_{31} + \lambda_{03}\lambda_{02} \\
& + \lambda_{13}\lambda_{12} + \lambda_{23}\lambda_{22} + \lambda_{33}\lambda_{32} - (\lambda_{01}\lambda_{02} + \lambda_{01}\lambda_{03} + \lambda_{01}\lambda_{12} + \lambda_{01}\lambda_{13} + \lambda_{01}\lambda_{22} + \lambda_{01}\lambda_{23} + \lambda_{01}\lambda_{32} \\
& + \lambda_{01}\lambda_{33} + 3\lambda_{01}\lambda_{01} + \lambda_{02}\lambda_{00} + \lambda_{12}\lambda_{10} + \lambda_{22}\lambda_{20} + \lambda_{32}\lambda_{30})] + d_1^2[2(\lambda_{01}\lambda_{00} + \lambda_{01}\lambda_{10} + \lambda_{01}\lambda_{11} \\
& + \lambda_{01}\lambda_{20} + \lambda_{01}\lambda_{21} + \lambda_{01}\lambda_{30} + \lambda_{01}\lambda_{31}) + 4(\lambda_{03}\lambda_{02} + \lambda_{13}\lambda_{12} + \lambda_{23}\lambda_{22} + \lambda_{33}\lambda_{32}) - (\lambda_{00}\lambda_{00} + \lambda_{10}\lambda_{10} \\
& + \lambda_{20}\lambda_{20} + \lambda_{30}\lambda_{30} + \lambda_{01}\lambda_{01} + \lambda_{11}\lambda_{11} + \lambda_{21}\lambda_{21} + \lambda_{31}\lambda_{31} + \lambda_{02}\lambda_{02} + \lambda_{12}\lambda_{12} + \lambda_{22}\lambda_{22} + \lambda_{32}\lambda_{32} \\
& + \lambda_{03}\lambda_{03} + \lambda_{13}\lambda_{13} + \lambda_{23}\lambda_{23} + \lambda_{33}\lambda_{33}) - 2(\lambda_{01}\lambda_{02} + \lambda_{01}\lambda_{03} + \lambda_{01}\lambda_{12} + \lambda_{01}\lambda_{13} + \lambda_{01}\lambda_{22} + \lambda_{01}\lambda_{23} \\
& + \lambda_{01}\lambda_{32} + \lambda_{01}\lambda_{33} + 3\lambda_{01}\lambda_{01} + \lambda_{03}\lambda_{00} + \lambda_{13}\lambda_{10} + \lambda_{23}\lambda_{20} + \lambda_{33}\lambda_{30})]\}, \tag{B5}
\end{aligned}$$

$$\begin{aligned}
\frac{d\lambda_{11}}{dl} = & \frac{1}{4\pi(d_3^2 + d_1^2)^{\frac{3}{2}}} \{2d_3^2[\lambda_{12}\lambda_{03} + \lambda_{13}\lambda_{02} + \lambda_{31}\lambda_{20} + \lambda_{30}\lambda_{21} + \lambda_{11}\lambda_{00} + \lambda_{11}\lambda_{01} + \lambda_{11}\lambda_{10} + \lambda_{11}\lambda_{22} + \lambda_{11}\lambda_{23} \\
& + \lambda_{11}\lambda_{32} + \lambda_{11}\lambda_{33} - (\lambda_{12}\lambda_{00} + \lambda_{10}\lambda_{02} + \lambda_{33}\lambda_{21} + \lambda_{31}\lambda_{23} + \lambda_{11}\lambda_{02} + \lambda_{11}\lambda_{03} + \lambda_{11}\lambda_{12} + \lambda_{11}\lambda_{13} + \lambda_{11}\lambda_{20} \\
& + \lambda_{11}\lambda_{21} + \lambda_{11}\lambda_{30} + \lambda_{11}\lambda_{31} + 3\lambda_{11}\lambda_{11})] + d_1^2[\lambda_{11}\lambda_{00} + \lambda_{11}\lambda_{01} + \lambda_{11}\lambda_{10} + \lambda_{11}\lambda_{22} + \lambda_{11}\lambda_{23} + \lambda_{11}\lambda_{32} + \lambda_{11}\lambda_{33}
\end{aligned}$$

$$\begin{aligned} \frac{d\lambda_{23}}{dl} = & \frac{1}{4\pi(d_3^2 + d_1^2)^{\frac{3}{2}}} \{2d_3^2[\lambda_{21}\lambda_{02} + \lambda_{22}\lambda_{01} + \lambda_{13}\lambda_{30} + \lambda_{10}\lambda_{33} - (\lambda_{20}\lambda_{00} + \lambda_{21}\lambda_{01} + \lambda_{22}\lambda_{02} + \lambda_{23}\lambda_{03})] + d_1^2[2(\lambda_{21}\lambda_{02} \\ & + \lambda_{22}\lambda_{01} + \lambda_{13}\lambda_{30} + \lambda_{10}\lambda_{33} + \lambda_{23}\lambda_{00} + \lambda_{23}\lambda_{03} + \lambda_{23}\lambda_{11} + \lambda_{23}\lambda_{12} + \lambda_{23}\lambda_{20} + \lambda_{23}\lambda_{31} + \lambda_{23}\lambda_{32}) - (\lambda_{22}\lambda_{00} \\ & + \lambda_{20}\lambda_{02} + \lambda_{13}\lambda_{31} + \lambda_{11}\lambda_{33} + \lambda_{21}\lambda_{00} + \lambda_{20}\lambda_{01} + \lambda_{12}\lambda_{33} + \lambda_{13}\lambda_{32}) - 2(\lambda_{23}\lambda_{01} + \lambda_{23}\lambda_{02} + \lambda_{23}\lambda_{10} + \lambda_{23}\lambda_{13} \\ & + \lambda_{23}\lambda_{21} + \lambda_{23}\lambda_{22} + \lambda_{23}\lambda_{30} + \lambda_{23}\lambda_{33} + 3\lambda_{23}\lambda_{23})]\}, \end{aligned} \quad (\text{B15})$$

$$\begin{aligned} \frac{d\lambda_{33}}{dl} = & \frac{1}{4\pi(d_3^2 + d_1^2)^{\frac{3}{2}}} \{2d_3^2[\lambda_{31}\lambda_{02} + \lambda_{32}\lambda_{01} + \lambda_{23}\lambda_{10} + \lambda_{20}\lambda_{13} - (\lambda_{30}\lambda_{00} + \lambda_{31}\lambda_{01} + \lambda_{32}\lambda_{02} + \lambda_{33}\lambda_{03})] + d_1^2[2(\lambda_{31}\lambda_{02} \\ & + \lambda_{32}\lambda_{01} + \lambda_{23}\lambda_{10} + \lambda_{20}\lambda_{13} + \lambda_{33}\lambda_{00} + \lambda_{33}\lambda_{03} + \lambda_{33}\lambda_{11} + \lambda_{33}\lambda_{12} + \lambda_{33}\lambda_{21} + \lambda_{33}\lambda_{22} + \lambda_{33}\lambda_{30}) - (\lambda_{32}\lambda_{00} \\ & + \lambda_{30}\lambda_{02} + \lambda_{23}\lambda_{11} + \lambda_{21}\lambda_{13} + \lambda_{31}\lambda_{00} + \lambda_{30}\lambda_{01} + \lambda_{22}\lambda_{13} + \lambda_{23}\lambda_{12}) - 2(\lambda_{33}\lambda_{01} + \lambda_{33}\lambda_{02} + \lambda_{33}\lambda_{10} + \lambda_{33}\lambda_{13} \\ & + \lambda_{33}\lambda_{20} + \lambda_{33}\lambda_{23} + \lambda_{33}\lambda_{31} + \lambda_{33}\lambda_{32} + 3\lambda_{33}\lambda_{33})]\}. \end{aligned} \quad (\text{B16})$$

Appendix C: RG equations of source terms

After collecting all the one-loop corrections to source terms and performing RG analysis [48, 51, 53], we can obtain RG flow equations of the strengths $\Delta_i^{c/s}$ and Δ_i^{PP} corresponding to fermion-source terms in particle-hole and particle-particle situations,

$$\frac{d\Delta_1^c}{dl} = 2\Delta_1^c, \quad (\text{C1})$$

$$\begin{aligned} \frac{d\Delta_2^c}{dl} = & \left[2 + (\lambda_{00} - 7\lambda_{01} - \lambda_{02} - \lambda_{03} + \lambda_{10} + \lambda_{11} - \lambda_{12} - \lambda_{13} + \lambda_{20} + \lambda_{21} - \lambda_{22} - \lambda_{23} + \lambda_{30} + \lambda_{31} \right. \\ & \left. - \lambda_{32} - \lambda_{33}) \frac{(2d_3^2 + d_1^2)}{16\pi(d_3^2 + d_1^2)^{\frac{3}{2}}} \right] \Delta_2^c, \end{aligned} \quad (\text{C2})$$

$$\begin{aligned} \frac{d\Delta_3^c}{dl} = & \left[2 + (\lambda_{00} - \lambda_{01} - 7\lambda_{02} - \lambda_{03} + \lambda_{10} - \lambda_{11} + \lambda_{12} - \lambda_{13} + \lambda_{20} - \lambda_{21} + \lambda_{22} - \lambda_{23} + \lambda_{30} - \lambda_{31} \right. \\ & \left. + \lambda_{32} - \lambda_{33}) \frac{(2d_3^2 + d_1^2)}{16\pi(d_3^2 + d_1^2)^{\frac{3}{2}}} \right] \Delta_3^c, \end{aligned} \quad (\text{C3})$$

$$\begin{aligned} \frac{d\Delta_4^c}{dl} = & \left[2 + (\lambda_{00} - \lambda_{01} - \lambda_{02} - 7\lambda_{03} + \lambda_{10} - \lambda_{11} - \lambda_{12} + \lambda_{13} + \lambda_{20} - \lambda_{21} - \lambda_{22} + \lambda_{23} + \lambda_{30} - \lambda_{31} \right. \\ & \left. - \lambda_{32} + \lambda_{33}) \frac{d_1^2}{8\pi(d_3^2 + d_1^2)^{\frac{3}{2}}} \right] \Delta_4^c, \end{aligned} \quad (\text{C4})$$

$$\frac{d\Delta_1^s}{dl} = 2\Delta_1^s, \quad (\text{C5})$$

$$\begin{aligned} \frac{d\Delta_{2-x}^s}{dl} = & \left[2 + (\lambda_{00} + \lambda_{01} - \lambda_{02} - \lambda_{03} + \lambda_{10} - 7\lambda_{11} - \lambda_{12} - \lambda_{13} - \lambda_{20} - \lambda_{21} + \lambda_{22} + \lambda_{23} - \lambda_{30} - \lambda_{31} \right. \\ & \left. + \lambda_{32} + \lambda_{33}) \frac{(2d_3^2 + d_1^2)}{16\pi(d_3^2 + d_1^2)^{\frac{3}{2}}} \right] \Delta_{2-x}^s, \end{aligned} \quad (\text{C6})$$

$$\begin{aligned} \frac{d\Delta_{2-y}^s}{dl} = & \left[2 + (\lambda_{00} + \lambda_{01} - \lambda_{02} - \lambda_{03} - \lambda_{10} - \lambda_{11} + \lambda_{12} + \lambda_{13} + \lambda_{20} - 7\lambda_{21} - \lambda_{22} - \lambda_{23} - \lambda_{30} - \lambda_{31} \right. \\ & \left. + \lambda_{32} + \lambda_{33}) \frac{(2d_3^2 + d_1^2)}{16\pi(d_3^2 + d_1^2)^{\frac{3}{2}}} \right] \Delta_{2-y}^s, \end{aligned} \quad (\text{C7})$$

$$\begin{aligned} \frac{d\Delta_{2-z}^s}{dl} = & \left[2 + (\lambda_{00} + \lambda_{01} - \lambda_{02} - \lambda_{03} - \lambda_{10} - \lambda_{11} + \lambda_{12} + \lambda_{13} - \lambda_{20} - \lambda_{21} + \lambda_{22} + \lambda_{23} + \lambda_{30} - 7\lambda_{31} \right. \\ & \left. - \lambda_{32} - \lambda_{33}) \frac{(2d_3^2 + d_1^2)}{16\pi(d_3^2 + d_1^2)^{\frac{3}{2}}} \right] \Delta_{2-z}^s, \end{aligned} \quad (\text{C8})$$

$$\begin{aligned} \frac{d\Delta_{3-x}^s}{dl} = & \left[2 + (\lambda_{00} - \lambda_{01} + \lambda_{02} - \lambda_{03} + \lambda_{10} - \lambda_{11} - 7\lambda_{12} - \lambda_{13} - \lambda_{20} + \lambda_{21} - \lambda_{22} + \lambda_{23} - \lambda_{30} + \lambda_{31} \right. \\ & \left. - \lambda_{32} + \lambda_{33}) \frac{(2d_3^2 + d_1^2)}{16\pi(d_3^2 + d_1^2)^{\frac{3}{2}}} \right] \Delta_{3-x}^s, \end{aligned} \quad (\text{C9})$$

$$\frac{d\Delta_{3-y}^s}{dl} = \left[2 + (\lambda_{00} - \lambda_{01} + \lambda_{02} - \lambda_{03} - \lambda_{10} + \lambda_{11} - \lambda_{12} + \lambda_{13} + \lambda_{20} - \lambda_{21} - 7\lambda_{22} - \lambda_{23} - \lambda_{30} + \lambda_{31} \right.$$

$$-\lambda_{32} + \lambda_{33}) \frac{(2d_3^2 + d_1^2)}{16\pi(d_3^2 + d_1^2)^{\frac{3}{2}}} \Big] \Delta_{3-y}^s, \quad (\text{C10})$$

$$\begin{aligned} \frac{d\Delta_{3-z}^s}{dl} = & \left[2 + (\lambda_{00} - \lambda_{01} + \lambda_{02} - \lambda_{03} - \lambda_{10} + \lambda_{11} - \lambda_{12} + \lambda_{13} - \lambda_{20} + \lambda_{21} - \lambda_{22} + \lambda_{23} + \lambda_{30} - \lambda_{31} \right. \\ & \left. - 7\lambda_{32} - \lambda_{33}) \frac{(2d_3^2 + d_1^2)}{16\pi(d_3^2 + d_1^2)^{\frac{3}{2}}} \right] \Delta_{3-z}^s, \end{aligned} \quad (\text{C11})$$

$$\begin{aligned} \frac{d\Delta_{4-x}^s}{dl} = & \left[2 + (\lambda_{00} - \lambda_{01} - \lambda_{02} + \lambda_{03} + \lambda_{10} - \lambda_{11} - \lambda_{12} - 7\lambda_{13} - \lambda_{20} + \lambda_{21} + \lambda_{22} - \lambda_{23} - \lambda_{30} + \lambda_{31} \right. \\ & \left. + \lambda_{32} - \lambda_{33}) \frac{d_1^2}{8\pi(d_3^2 + d_1^2)^{\frac{3}{2}}} \right] \Delta_{4-x}^s, \end{aligned} \quad (\text{C12})$$

$$\begin{aligned} \frac{d\Delta_{4-y}^s}{dl} = & \left[2 + (\lambda_{00} - \lambda_{01} - \lambda_{02} + \lambda_{03} - \lambda_{10} + \lambda_{11} + \lambda_{12} - \lambda_{13} + \lambda_{20} - \lambda_{21} - \lambda_{22} - 7\lambda_{23} - \lambda_{30} + \lambda_{31} \right. \\ & \left. + \lambda_{32} - \lambda_{33}) \frac{d_1^2}{8\pi(d_3^2 + d_1^2)^{\frac{3}{2}}} \right] \Delta_{4-y}^s, \end{aligned} \quad (\text{C13})$$

$$\begin{aligned} \frac{d\Delta_{4-z}^s}{dl} = & \left[2 + (\lambda_{00} - \lambda_{01} - \lambda_{02} + \lambda_{03} - \lambda_{10} + \lambda_{11} + \lambda_{12} - \lambda_{13} - \lambda_{20} + \lambda_{21} + \lambda_{22} - \lambda_{23} + \lambda_{30} - \lambda_{31} \right. \\ & \left. - \lambda_{32} - 7\lambda_{33}) \frac{d_1^2}{8\pi(d_3^2 + d_1^2)^{\frac{3}{2}}} \right] \Delta_{4-z}^s, \end{aligned} \quad (\text{C14})$$

and

$$\begin{aligned} \frac{d\Delta_1^{\text{PP}}}{dl} = & \left\{ 2 + \left[\lambda_{01} + \lambda_{10} + \lambda_{12} + \lambda_{13} + \lambda_{20} + \lambda_{22} + \lambda_{23} + \lambda_{30} + \lambda_{32} + \lambda_{33} - (\lambda_{00} + \lambda_{02} + \lambda_{03} + \lambda_{11} \right. \right. \\ & \left. \left. + \lambda_{21} + \lambda_{31}) \right] \frac{d_3^2}{8\pi(d_3^2 + d_1^2)^{\frac{3}{2}}} \right\} \Delta_1^{\text{PP}}, \end{aligned} \quad (\text{C15})$$

$$\begin{aligned} \frac{d\Delta_2^{\text{PP}}}{dl} = & \left\{ 2 + \left[\lambda_{03} + \lambda_{10} + \lambda_{11} + \lambda_{12} + \lambda_{20} + \lambda_{21} + \lambda_{22} + \lambda_{30} + \lambda_{31} + \lambda_{32} - (\lambda_{00} + \lambda_{01} + \lambda_{02} + \lambda_{13} \right. \right. \\ & \left. \left. + \lambda_{23} + \lambda_{33}) \right] \frac{d_1^2}{16\pi(d_3^2 + d_1^2)^{\frac{3}{2}}} \right\} \Delta_2^{\text{PP}}, \end{aligned} \quad (\text{C16})$$

$$\begin{aligned} \frac{d\Delta_3^{\text{PP}}}{dl} = & \left\{ 2 + \left[\lambda_{02} + \lambda_{10} + \lambda_{11} + \lambda_{13} + \lambda_{20} + \lambda_{21} + \lambda_{23} + \lambda_{30} + \lambda_{31} + \lambda_{33} - (\lambda_{00} + \lambda_{01} + \lambda_{03} + \lambda_{12} \right. \right. \\ & \left. \left. + \lambda_{22} + \lambda_{32}) \right] \frac{1}{8\pi(d_3^2 + d_1^2)^{\frac{1}{2}}} \right\} \Delta_3^{\text{PP}}, \end{aligned} \quad (\text{C17})$$

$$\begin{aligned} \frac{d\Delta_{4-x}^{\text{PP}}}{dl} = & \left\{ 2 + \left[\lambda_{01} + \lambda_{02} + \lambda_{03} + \lambda_{11} + \lambda_{12} + \lambda_{13} + \lambda_{20} + \lambda_{31} + \lambda_{32} + \lambda_{33} - (\lambda_{00} + \lambda_{10} + \lambda_{21} + \lambda_{22} \right. \right. \\ & \left. \left. + \lambda_{23} + \lambda_{30}) \right] \frac{d_1^2}{16\pi(d_3^2 + d_1^2)^{\frac{3}{2}}} \right\} \Delta_{4-x}^{\text{PP}}, \end{aligned} \quad (\text{C18})$$

$$\begin{aligned} \frac{d\Delta_{4-y}^{\text{PP}}}{dl} = & \left\{ 2 + \left[\lambda_{01} + \lambda_{02} + \lambda_{03} + \lambda_{11} + \lambda_{12} + \lambda_{13} + \lambda_{21} + \lambda_{22} + \lambda_{23} + \lambda_{30} - (\lambda_{00} + \lambda_{10} + \lambda_{20} + \lambda_{31} \right. \right. \\ & \left. \left. + \lambda_{32} + \lambda_{33}) \right] \frac{d_1^2}{16\pi(d_3^2 + d_1^2)^{\frac{3}{2}}} \right\} \Delta_{4-y}^{\text{PP}}, \end{aligned} \quad (\text{C19})$$

$$\begin{aligned} \frac{d\Delta_{4-z}^{\text{PP}}}{dl} = & \left\{ 2 + \left[\lambda_{01} + \lambda_{02} + \lambda_{03} + \lambda_{10} + \lambda_{21} + \lambda_{22} + \lambda_{23} + \lambda_{31} + \lambda_{32} + \lambda_{33} - (\lambda_{00} + \lambda_{11} + \lambda_{12} + \lambda_{13} \right. \right. \\ & \left. \left. + \lambda_{20} + \lambda_{30}) \right] \frac{d_1^2}{16\pi(d_3^2 + d_1^2)^{\frac{3}{2}}} \right\} \Delta_{4-z}^{\text{PP}}, \end{aligned} \quad (\text{C20})$$

where the right hand sides of these equations are designated as $\mathcal{G}_i^{c/s, \text{PP}} \Delta_i^{c/s, \text{PP}}$ in Eq. (14).

[1] K. S. Novoselov, A. K. Geim, S. V. Morozov, D. Jiang, M. I. Katsnelson, I. V. Grigorieva, S. V. Dubonos, and

A. A. Firsov, Nature **438**, 197 (2005).

- [2] A. H. Castro Neto, F. Guinea, N. M. R. Peres, K. S. Novoselov, and A. K. Geim, *Rev. Mod. Phys.* **81**, 109 (2009).
- [3] L. Fu, C. L. Kane, and E. J. Mele, *Phys. Rev. Lett.* **98**, 106803 (2007).
- [4] R. Roy, *Phys. Rev. B* **79**, 195322 (2009).
- [5] J. E. Moore, *Nature* **464**, 194 (2010).
- [6] M. Z. Hasan and C. L. Kane, *Rev. Mod. Phys.* **82**, 3045 (2010).
- [7] X. L. Qi and S. C. Zhang, *Rev. Mod. Phys.* **83**, 1057 (2011).
- [8] S. Q. Sheng, *Dirac Equation in Condensed Matter* (Berlin: Springer, 2012).
- [9] B. A. Bernevig and T. L. Hughes, *Topological Insulators and Topological Superconductors* (Princeton, NJ: Princeton University Press, 2013).
- [10] N. P. Armitage, E. J. Mele, and Ashvin Vishwanath, *Rev. Mod. Phys.* **90**, 015001 (2018).
- [11] B. Roy and M. S. Foster, *Phys. Rev. X* **8**, 011049 (2018).
- [12] H. K. Tang, J. N. Leaw, J. N. B. Rodrigues, I. F. Herbut, P. Sengupta, F. F. Assaad, and S. Adam, *Science* **361**, 570 (2018).
- [13] M. M. Korshunov, D. V. Efremov, A. A. Golubov, and O. V. Dolgov, *Phys. Rev. B* **90**, 134517 (2014).
- [14] H. H. Hung, A. Barr, E. Prodan, and G. A. Fiete, *Phys. Rev. B* **94**, 235132 (2016).
- [15] R. Nandkishore, J. Maciejko, D. A. Huse, and S. L. Sondhi, *Phys. Rev. B* **87**, 174511 (2013).
- [16] I. D. Potirniche, J. Maciejko, R. Nandkishore, and S. L. Sondhi, *Phys. Rev. B* **90**, 094516 (2014).
- [17] B. Roy and S. Das Sarma, *Phys. Rev. B* **94**, 115137 (2016).
- [18] R. M. Nandkishore and S. A. Parameswaran, *Phys. Rev. B* **95**, 205106 (2017).
- [19] B. Roy, Y. Alavirad, and J. D. Sau, *Phys. Rev. Lett.* **118**, 227002 (2017).
- [20] B. Roy, R. J. Slager, and V. Juričić, *Phys. Rev. X* **8**, 031076 (2018).
- [21] B. Roy, V. Juričić, and S. D. Sarma, *Sci. Rep.* **6**, 32446 (2016).
- [22] Z. J. Wang, Y. Sun, X. Q. Chen, C. Franchini, G. Xu, H. M. Weng, X. Dai, and Z. Fang, *Phys. Rev. B* **85**, 195320 (2012).
- [23] S. M. Young, S. Zaheer, J. C. Y. Teo, C. L. Kane, E. J. Mele, and A. M. Rappe, *Phys. Rev. Lett.* **108**, 140405 (2012).
- [24] J. A. Steinberg, S. M. Young, S. Zaheer, C. L. Kane, E. J. Mele, and A. M. Rappe, *Phys. Rev. Lett.* **112**, 036403 (2014).
- [25] Z. K. Liu, J. Jiang, B. Zhou, Z. J. Wang, Y. Zhang, H. M. Weng, D. Prabhakaran, S. K. Mo, H. Peng, P. Dudin, T. Kim, M. Hoesch, Z. Fang, X. Dai, Z. X. Shen, D. L. Feng, Z. Hussain, and Y. L. Chen, *Nat. Mater.* **13**, 677 (2014).
- [26] Z. K. Liu, B. Zhou, Y. Zhang, Z. J. Wang, H. M. Weng, D. Prabhakaran, S. K. Mo, Z. X. Shen, Z. Fang, X. Dai, Z. Hussain, and Y. L. Chen, *Science* **343**, 864 (2014).
- [27] J. Xiong, S. K. Kushwaha, T. Liang, J. W. Krizan, M. Hirschberger, W. Wang, R. J. Cava, and N. P. Ong, *Science* **350**, 413 (2015).
- [28] A. A. Burkov and L. Balents, *Phys. Rev. Lett.* **107**, 127205 (2011).
- [29] K. Y. Yang, Y. M. Lu, and Y. Ran, *Phys. Rev. B* **84**, 075129 (2011).
- [30] X. G. Wan, A. M. Turner, A. Vishwanath, and S. Y. Savrasov, *Phys. Rev. B* **83**, 205101 (2011).
- [31] X. C. Huang, L. X. Zhao, Y. J. Long, P. P. Wang, D. Chen, Z. H. Yang, H. Liang, M. Q. Xue, H. M. Weng, Z. Fang, X. Dai, and G. F. Chen, *Phys. Rev. X* **5**, 031023 (2015).
- [32] S. Y. Xu, I. Belopolski, N. Alidoust, M. Neupane, G. Bian, C. L. Zhang, R. Sankar, G. Q. Chang, Z. J. Yuan, C. C. Lee, S. M. Huang, H. Zheng, J. Ma, D. S. Sanchez, B. K. Wang, A. Bansil, F. C. Chou, P. P. Shibayev, H. Lin, S. Jia, and M. Z. Hasan, *Science* **349**, 613 (2015).
- [33] S. Y. Xu, N. Alidoust, I. Belopolski, Z. J. Yuan, G. Bian, T. R. Chang, H. Zheng, V. N. Strocov, D. S. Sanchez, G. Q. Chang, C. L. Zhang, D. X. Mou, Y. Wu, L. Huang, C. C. Lee, S. M. Huang, B. K. Wang, A. Bansil, H. T. Jeng, T. Neupert, A. Kaminski, H. Lin, S. Jia, and M. Z. Hasan, *Nat. Phys.* **11**, 748 (2015).
- [34] B. Q. Lv, N. Xu, H. M. Weng, J. Z. Ma, P. Richard, X. C. Huang, L. X. Zhao, G. F. Chen, C. E. Matt, F. Bisti, V. N. Strocov, J. Mesot, Z. Fang, X. Dai, T. Qian, M. Shi, and H. Ding, *Nat. Phys.* **11**, 724 (2015).
- [35] H. Weng, C. Fang, Z. Fang, B. A. Bernevig, and X. Dai, *Phys. Rev. X* **5**, 011029 (2015).
- [36] Y. Hasegawa, R. Konno, H. Nakano, and M. Kohmoto, *Phys. Rev. B* **74**, 033413 (2006).
- [37] S. Katayama, A. Kobayashi, and Y. Suzumura, *J. Phys. Soc. Japan* **75**, 054705 (2006).
- [38] P. Dietl, F. Piechon, and G. Montambaux, *Phys. Rev. Lett.* **100**, 236405 (2008).
- [39] V. Pardo and W. E. Pickett, *Phys. Rev. Lett.* **102**, 166803 (2009).
- [40] P. Delplace and G. Montambaux, *Phys. Rev. B* **82**, 035438 (2010).
- [41] Y. Wu, *Opt. Express* **22**, 1906 (2014).
- [42] Y. D. Chong, X. G. Wen, and M. Soljačić, *Phys. Rev. B* **77**, 235125 (2008).
- [43] K. Sun and E. Fradkin, *Phys. Rev. B* **78**, 245122 (2008).
- [44] K. Sun, H. Yao, E. Fradkin, and S. A. Kivelson, *Phys. Rev. Lett.* **103**, 046811 (2009).
- [45] O. Vafek, *Phys. Rev. B* **82**, 205106 (2010).
- [46] O. Vafek and K. Yang, *Phys. Rev. B* **81**, 041401(R) (2010).
- [47] V. Cvetković, R. E. Throckmorton, and O. Vafek, *Phys. Rev. B* **86**, 075467 (2012).
- [48] J. M. Murray and O. Vafek, *Phys. Rev. B* **89**, 201110(R) (2014).
- [49] I. F. Herbut, *Phys. Rev. B* **85**, 085304 (2012).
- [50] W. Zhu, S. S. Gong, T. S. Zeng, L. Fu, and D. N. Sheng, *Phys. Rev. Lett.* **117**, 096402 (2016).
- [51] J. Wang, C. Ortix, J. van den Brink, and D. V. Efremov, *Phys. Rev. B* **96**, 201104(R) (2017).
- [52] Y. M. Dong, Y. H. Zhai, D. X. Zheng, and J. Wang, *Phys. Rev. B* **102**, 134204 (2020).
- [53] B. Roy, arxiv: 2004.13043 (2020).
- [54] I. Mandal and S. Gemsheim, *Condens. Matter Phys.* **22**, 13701 (2019).
- [55] S. Ray, M. Vojta, and L. Janssen, *Phys. Rev. B* **102**, 081112(R) (2020).
- [56] J. Shah and S. Mukerjee, arxiv: 2011.00249 (2020).
- [57] I. Mandal and R. M. Nandkishore, *Phys. Rev. B* **97**, 125121 (2018).
- [58] Y. P. Lin and R. M. Nandkishore,

- Phys. Rev. B **97**, 134521 (2018).
- [59] J. M. Luttinger, Phys. Rev. **102**, 1030 (1956).
- [60] S. Murakami, N. Nagaosa, and S. C. Zhang, Phys. Rev. B **69**, 235206 (2004).
- [61] L. Janssen and I. F. Herbut, Phys. Rev. B **92**, 045117 (2015).
- [62] I. Boettcher and I. F. Herbut, Phys. Rev. B **93**, 205138 (2016).
- [63] L. Janssen and I. F. Herbut, Phys. Rev. B **95**, 075101 (2017).
- [64] I. Boettcher and I. F. Herbut, Phys. Rev. B **95**, 075149 (2017).
- [65] L. Savary, E. G. Moon, and L. Balents, Phys. Rev. X **4**, 041027 (2014).
- [66] L. Savary, J. Ruhman, J. W. F. Venderbos, L. Fu, and P. A. Lee, Phys. Rev. B **96**, 214514 (2017).
- [67] H. H. Lai, B. Roy, and P. Goswami, arXiv: 1409.8675 (2014).
- [68] P. Goswami, B. Roy, and S. Das Sarma, Phys. Rev. B **95**, 085120 (2017).
- [69] A. L. Szabo, R. Moessner, and B. Roy, arXiv:1811.12415 (2018).
- [70] B. Roy, Sayed Ali Akbar Ghorashi, M. S. Foster, and A. H. Nevidomskyy, Phys. Rev. B **99**, 054505 (2019).
- [71] S. Ray, M. Vojta, and L. Janssen, Phys. Rev. B **98**, 245128 (2018).
- [72] J. R. Wang, W. Li, and C. J. Zhang, Phys. Rev. B **102**, 085132 (2020).
- [73] G. W. Chern and C. D. Batista, Phys. Rev. Lett. **109**, 156801 (2012).
- [74] W. F. Tsai, C. Fang, H. Yao, and J. Hu, New J. Phys. **17**, 055016 (2015).
- [75] Y. Xiao, V. Pelletier, P. M. Chaikin, and D. A. Huse, Phys. Rev. B **67**, 104505 (2003).
- [76] J. W. F. Venderbos, M. Manzardo, D. V. Efremov, J. van den Brink, and C. Ortix, Phys. Rev. B **93**, 045428 (2016).
- [77] H. Q. Wu, Y. Y. He, C. Fang, Z. Y. Meng, and Z. Y. Lu, Phys. Rev. Lett. **117**, 066403 (2016).
- [78] R. Shankar, Rev. Mod. Phys. **66**, 129 (1994).
- [79] K. G. Wilson, Rev. Mod. Phys. **47**, 773 (1975).
- [80] J. Polchinski, arXiv: hep-th/9210046 (1992).
- [81] S. Maiti and A. V. Chubukov, Phys. Rev. B **82**, 214515 (2010).
- [82] A. Altland and B. Simons, *Condensed Matter Field Theory* (Cambridge University Press, Cambridge, 2006).
- [83] M. Vojta, Rep. Prog. Phys. **66**, 2069 (2003).
- [84] C. J. Halboth and W. Metzner, Phys. Rev. Lett. **85**, 5162 (2000).
- [85] C. J. Halboth and W. Metzner, Phys. Rev. B **61**, 7364 (2000).
- [86] J. Wang, A. Eberlein, and W. Metzner, Phys. Rev. B **89**, 121116(R) (2014).
- [87] A. V. Chubukov, Annu. Rev. Condens. Matter Phys. **3**, 57 (2012).
- [88] A. V. Chubukov, M. Khodas, and R. M. Fernandes, Phys. Rev. X **6**, 041045 (2016).
- [89] J. Wang and G. Z. Liu, Phys. Rev. D **85**, 105010 (2012).
- [90] A. Altland, B. D. Simons, and M. R. Zirnbauer, Phys. Rep. **359**, 283 (2002).
- [91] A. W. W. Ludwig, M. P. A. Fisher, R. Shankar, and G. Grinstein, Phys. Rev. B **50**, 7526 (1994).
- [92] C. Xu, Y. Qi, and S. Sachdev, Phys. Rev. B **78**, 134507 (2008).
- [93] J. R. Wang, G. Z. Liu, and C. J. Zhang, New J. Phys. **18**, 073023 (2016).
- [94] J. Wang, P. L. Zhao, J. R. Wang, and G. Z. Liu, Phys. Rev. B **95**, 054507 (2017).
- [95] Y. M. Dong, D. X. Zheng, and J. Wang, J. Phys.: Condens. Matter. **31**, 275601 (2019).
- [96] J. Wang, J. Phys: Condens. Matter. **30**, 125401 (2018).
- [97] J. Wang, G. Z. Liu, and H. Kleinert, Phys. Rev. B **83**, 214503 (2011).
- [98] Y. Huh and S. Sachdev, Phys. Rev. B **78**, 064512 (2008).
- [99] J. Wang, Phys. Rev. B. **87**, 054511 (2013).
- [100] J. H. She, J. Zaanen, A. R. Bishop, and A. V. Balatsky, Phys. Rev. B **82**, 165128 (2010).
- [101] E. A. Kim, M. J. Lawler, P. Oreto, S. Sachdev, E. Fradkin, and S. A. Kivelson, Phys. Rev. B. **77**, 184514 (2008).
- [102] J. H. She, M. J. Lawler, and E. A. Kim, Phys. Rev. B. **92**, 035112 (2015).
- [103] B. Roy, P. Goswami, and J. D. Sau, Phys. Rev. B. **94**, 041101(R) (2016).
- [104] T. Stauber, F. Guinea, and M. A. H. Vozmediano, Phys. Rev. B **71**, 041406(R) (2005).
- [105] R. Nandkishore, L. S. Levitov, and A. V. Chubukov, Nat. Phys. **8**, 158 (2012).
- [106] A. L. Szabó and B. Roy, arXiv: 2009.05055 (2020).
- [107] J. Wang, Nuclear Physics B **961**, 115230 (2020).
- [108] Y. P. Lin and R. M. Nandkishore, arXiv: 2008.05485 (2020).
- [109] R. E. Peierls, *Quantum theory of solids*, 23 (Oxford University Press, 1955).
- [110] V. Saran, M. Karmakar, and R. Ganesh, Phys. Rev. B **100**, 104520 (2019).
- [111] Y. Tada, Phys. Rev. Research **2**, 033363 (2020).
- [112] M. J. Trott and C. A. Hooley, arXiv: 2004.06665 (2020).
- [113] D. Sehayek, M. Thakurathi, and A. A. Burkov, Phys. Rev. B **102**, 115159 (2020).
- [114] P. A. Lee, N. Nagaosa, and X. G. Wen, Rev. Mod. Phys. **78**, 17 (2006).
- [115] E. Fradkin, S. A. Kivelson, M. J. Lawler, J. P. Eisenstein, and A. P. Mackenzie, Annu. Rev. Condens. Matter Phys. **1**, 153 (2010).
- [116] S. Das Sarma, S. Adam, E. H. Hwang, and E. Rossi, Rev. Mod. Phys. **83**, 407 (2011).
- [117] S. Sachdev, *Quantum Phase Transitions 2nd edn* (Cambridge: Cambridge University Press, 2011).
- [118] V. N. Kotov, B. Uchoa, V. M. Pereira, F. Guinea, and A. H. Castro Neto, Rev. Mod. Phys. **84**, 1067 (2012).
- [119] G. Mahan, *Many-Particle Physics, 2nd edn.* (Plenum, New York, 1990).
- [120] J. I. Kapusta and C. Gale, *Finite-Temperature Field Theory: Principles and Applications* (Cambridge, UK; New York, 1994).
- [121] I. S. Gradshteyn and I. M. Ryzhik, *Table of Integrals, Series, and Products, 7th edn.* (Academic Press, America, 2007).
- [122] D. E. Sheehy and J. Schmalian, Phys. Rev. Lett. **99**, 226803 (2007).
- [123] F. Schwabl, *Statistical Mechanics* (Springer, Berlin, 2006), 2nd ed., p. 85.
- [124] E. H. Hwang, Ben Yu-Kuang Hu, and S. Das Sarma, Phys. Rev. Lett. **99**, 226801 (2007).